

Large-Eddy Simulation of combustion instabilities in a lean partially premixed swirled flame

B. Franzelli ^{a,*}, E. Riber ^a, L.Y.M. Giquel ^a and T. Poinsot ^b

^aCERFACS, CFD Team, 42 Avenue G. Coriolis, 31057 Toulouse Cedex 01, France

^bIMFT-UMR 5502, allée du Professeur Camille Soula, 31400 Toulouse, France

Abstract

This paper investigates one issue related to Large Eddy Simulation (LES) of self-excited combustion instabilities in gas-fueled swirled burners: the effects of incomplete mixing between fuel and air at the combustion chamber inlet. Perfect premixing of the gases entering the combustion chamber is rarely achieved in practical applications and this study investigates its impact by comparing LES assuming perfect premixing and LES where the fuel jets are resolved so that fuel/air mixing is explicitly computed. This is done for the Preccinsta swirled burner which has been carefully studied experimentally at DLR. All previous LES studies of Preccinsta have assumed perfect premixing and this work demonstrates that this assumption is reasonable for stable flows but is not acceptable to predict self-excited unstable cases. This is shown by comparing LES and experimental fields in terms of mean and RMS fields of temperature, species and velocities as well as mixture fraction pdfs and unsteady activity for two regimes: a stable one at equivalence ratio 0.83 and an unstable one at 0.7.

Key words: Gas turbines; Turbulent non-perfectly premixed combustion; Large

* Corresponding author.

Address: CERFACS, CFD Team, 42 Avenue G. Coriolis, 31057 Toulouse Cedex 01,
France.

Tel: +33 (0)5 61 19 30 83; fax: +33 (0)5 61 19 30 00.

Email address: franzell@cerfacs.fr (B. Franzelli).

Introduction

The instabilities of swirled turbulent flows have been the subject of intense research in the last ten years. One important issue has been to identify the possibilities offered by simulation and especially Large Eddy Simulation (LES) to predict self-excited combustion oscillations. The specific example of swirled combustors where flames couple with acoustic modes has received significant attention [1–4] because such oscillations are often found in real gas turbines [5,6]. An important question in swirled unstable flames is the effect of mixing on stability. In most real systems, combustion is not fully premixed and even in laboratories, very few swirled flames are truly fully premixed. The effects of equivalence ratio fluctuations on flame stability in combustors have been known for a long time [7,8]: changes in air inlet velocity induce variations of the flow rate through the flame but may also induce mixing fluctuations and the introduction into the combustion zone of non-constant equivalence ratio pockets. These pockets create unsteady combustion and can generate instabilities.

In many experiments, LES is performed assuming perfect mixing mainly because the computational work is simpler: there is no need to mesh the fuel injection holes or to resolve the zone where these jets mix with air. However, this assumption totally eliminates fluctuations of equivalence ratio as a mechanism of instability, thereby limiting the validity of the LES. One specific example of such limitations is the Preccinsta experiment which has been operated at DLR [9–11] and computed by multiple groups [12–16]. This methane/air swirled combustor was especially built to study combustion instabilities in such systems and for all computations up to now, perfect

mixing has been assumed by LES experts because methane was injected in the swirler, far upstream of the combustor, suggesting that perfect mixing was achieved in the combustion zone. Interestingly, all computations performed with perfect mixing assumptions have failed to predict the unstable modes observed in the experiments. Moreover, recent Laser Raman scattering measurements at DLR [11] have shown that mixing was not perfect in the chamber and suggested that incomplete mixing could be the source of the instability observed for a mean operating equivalence ratio smaller than $\phi = 0.75$.

The objective of the present work is to use LES to investigate the effects of mixing on the Preccinsta combustor. The unstructured grid is sufficiently fine to resolve the methane jets and perform both perfectly premixed and real methane injection simulations. Comparing these simulations to experimental results of DLR provides a clear description of the effects of the perfectly premixed assumption. Results show that resolving the mixing of methane and air allows to obtain better mean flow statistics, more realistic Probability Density Functions (pdf) of mixing within the combustor and most importantly, to predict when the combustor becomes unstable. Section 1 presents the experimental setup and discusses the most important experimental results. Section 2 describes the numerical setup used for the LES (chemical scheme, mesh, boundary conditions). Section 3 presents the results for a 'quiet' flame at equivalence ratio $\phi = 0.83$ and a 'pulsating' flame at $\phi = 0.7$. LES results for the two regimes are compared to experimental data in terms of mean and root mean square (RMS) temperature, species and velocity fields, unsteady activity, and pdf of mixture fraction. Even though a further improved LES of the Preccinsta experiment would involve many other in-

gradients (a finer mesh, more precise chemical schemes, radiation model, wall heat loss description), present results demonstrate that a proper LES of this configuration must include the methane jets and can not be performed with a fully perfect mixing assumption.

1 The swirled premixed burner Preccinsta

The Preccinsta experimental burner has been widely described and studied experimentally [9–11] but also numerically [12–16]. It is derived from an industrial design by Turbomeca and its behaviour is representative of an industrial gas turbine combustor. Two different regimes have been detected experimentally in this swirled combustor: a 'quiet' and a 'pulsating' flame.

The combustor can be divided into four distinct parts (Fig. 1). The first part is the plenum, where dry air at ambient temperature is injected through one large hole. The second part is the injector, where the air flow is swirled by twelve radial vanes. Methane is injected into the air flow through twelve small holes (one for each vane) of 1 mm diameter within the radial swirler. The high momentum flow of the swirler is supposed to ensure a good mixing of air and fuel before the nozzle exit. The exit plane of the nozzle is defined as $h = 0$ for all measurements. The third part of the configuration is the combustion chamber which has a square cross section ($85 \times 85 \text{ mm}^2$) and is equipped with 1.5 mm thick quartz walls to enable optical measurements. The fourth part is a converging duct which connects the combustor to the atmosphere.

Two different regimes have been experimentally observed [11]:

- **Case 1:** For a global equivalence ratio of $\phi = 0.7$, an unsteady pulsating flame is detected at a frequency $f = 290 \text{ Hz}$.
- **Case 2a:** For a global equivalence ratio of $\phi = 0.83$, a quiet and stable flame is observed in the combustion chamber.

For both cases, Laser Doppler Velocimetry (LDV) measurements of the velocity field were performed in vertical planes located at five different axial sections ($h = 1.5, 5, 15, 25$ and 35 mm) and along the radial direction. Note that the LDV measurements for the 'quiet' flame correspond to slightly different conditions (case 2b in Table 1), *i.e.* a global equivalence ratio of $\phi = 0.75$, and they are not useful for a direct comparison with the numerical results. Systematic and statistical uncertainties are less than 0.5% and 2% respectively [11]. The burner operating conditions of all cases are summarized in Table 1.

Laser Raman scattering is used in both cases 1 and 2a to obtain quantitative measurements of major species ($\text{CH}_4, \text{O}_2, \text{N}_2, \text{CO}, \text{CO}_2, \text{H}_2\text{O}$ and H_2) and temperature in vertical planes at eight different sections downstream of the injector ($h = 6, 10, 15, 20, 30, 40, 60$ and 80 mm). The systematic and statistical uncertainties are less than 4% and 2.5% respectively for temperature and less than 5% and 7% respectively for almost all species. For CO and H_2 , the statistical uncertainty is between 20 – 50%.

Raman measurements were analyzed [11] in front of the swirler exit to characterize methane/air mixing in the Inner Recirculation Zone (IRZ) and evaluate equivalence ratio fluctuations that can be a source of combustion instabilities. Although the fuel injection was designed to provide an efficient

mixing between air and fuel at the chamber inlet, a comparison between the 'quiet' and the 'pulsating' flame suggest that mixing in the chamber is not perfect and that the fluctuations of equivalence ratio can be the source of the instabilities. Figure 2 displays the experimental correlation between temperature and mixture fraction (noted z and based on Bilger's definition [17]) for the 'quiet' ($\phi = 0.83$) and the 'pulsating' ($\phi = 0.7$) cases. The mixture fraction distribution suggests that mixing is not perfect and that its variation is bigger for the 'pulsating' flame at $\phi = 0.7$. Experiments also suggest that this fluctuation is linked to an oscillation of the methane supply. One conclusion is thus that this oscillation generates a variation of combustion intensity, which in turn triggers the pressure oscillation. This effect is higher at $\phi = 0.7$ than at $\phi = 0.83$.

As a consequence, describing mixing before the nozzle exit is necessary to predict the instabilities when performing LES. The hypothesis of perfect premixing used in all previous simulations of the Preccinsta burner seems to be too restrictive and the evaluation of its impact is analyzed with LES in the following sections.

2 Large Eddy simulation for gas turbines

Four different simulations (Table 2) have been performed to study the impact of mixing on the instabilities. Cases A and C correspond to the 'quiet' and 'pulsating' flames, for which perfect premixing is assumed in LES: a perfectly premixed mixture of methane and dry air at the studied equivalence ratio is injected directly in the plenum (no fuel is injected through

the twelve holes in the swirler). In cases B and D, respectively corresponding to the 'quiet' and 'pulsating' flames, LES are computed without the perfect mixing assumption and match exactly the experimental setup: dry air is injected in the plenum and mixes in the swirler with the methane injected through the twelve injection holes. To allow a direct comparison of all simulations, all cases are calculated on the same mesh and with the same numerical parameters.

2.1 *The 2S_CH4_BFER mechanism for premixed methane/air flames*

The LES are performed using a two-step reduced scheme for laminar premixed methane/air flames called 2S_CH4_BFER. It contains six species (CH_4 , O_2 , N_2 , CO , CO_2 and H_2O) and has been built using the methodology described in [18] for premixed kerosene-air flames.

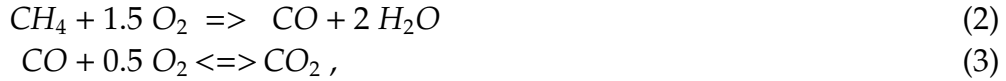
Simple models for transport and thermodynamic properties are used. A constant Prandtl number $Pr_o = \mu c_p / \lambda$ is assumed, where ρ is the gas mixture density, c_p is the gas mixture specific heat capacity at constant pressure, λ is the gas mixture thermal conductivity, and μ is the gas mixture dynamic viscosity following a power law:

$$\mu(T) = \mu_o \left(\frac{T}{T_o} \right)^\alpha . \quad (1)$$

The Prandtl number $Pr_o = 0.7$ and the reference dynamic viscosity $\mu_o = 1.8405 \cdot 10^{-5} \text{ kg/m/s}$ result from the GRI 3.0 detailed mechanism [19] involving 53 species and 341 reactions. They correspond to the Prandtl number and dynamic viscosity in the burnt gases at the reference temperature $T_o = 300\text{K}$ whereas the exponent $\alpha = 0.6759$ enables to fit the temperature dependency of the dynamic viscosity over the whole range of temperature at atmospheric

pressure [6]. Moreover, the unity Lewis number assumption for all species is used, which does not affect much the laminar flame structure for light fuels [18] and is consistent with the other simplifications used for molecular transport and thermodynamic data.

The 2S_CH4_BFER scheme is based on the two following reactions:



where the forward reaction rates for reactions (2) and (3) are written as:

$$k_{f,1} = A_1 f_1(\phi) T^{\beta_1} e^{(-E_{a,1}/RT)} [CH_4]^{n_{CH_4}} [O_2]^{n_{O_2,1}} , \quad (4)$$

$$k_{f,2} = A_2 f_2(\phi) T^{\beta_2} e^{(-E_{a,2}/RT)} [CO]^{n_{CO}} [O_2]^{n_{O_2,2}} , \quad (5)$$

where A_k is the pre-exponential factor, $E_{a,k}$ the activation energy, β_k the temperature exponent of reaction k and $n_{j,k}$ the reaction exponent for species j in reaction k . The subscripts 1 and 2 respectively denote the methane oxidation and the $CO - CO_2$ equilibrium reactions. The reaction parameters are summarised in Table 3.

The reaction exponents $n_{j,k}$ have been chosen following [6] so that the obtained pressure exponent $\alpha_p = (n_{CH_4} + n_{O_2} - 2) / 2$ is almost equal to the mean value over the whole range of pressure, temperature and equivalence ratio considered: $\alpha_p = -0.425$. Note that this pressure dependent coefficient is not constant [20], varying from $\alpha_p = -0.53$ for $T_f = 300$ K and $P = 10$ atm, to $\alpha_p = -0.29$ at $T_f = 700$ K and $P = 3$ atm using the GRI 3.0 mechanism.

The first reaction controls the flame speed and the autoignition time. The second reaction represents the $CO - CO_2$ equilibrium and is necessary to predict the flame temperature in the burnt gases for rich mixtures.

The two pre-exponential factors are adjusted by two correction functions depending on local equivalence ratio: f_1 allows to decrease the laminar flame speed for rich flames, bringing the flame speed to the GRI 3.0 mechanism values whereas f_2 is calibrated to adjust the thickness of the post-flame zone and to quickly reach the equilibrium state. The two correction functions are given by:

$$f_1(\phi) = \frac{2}{\left[1 + \tanh\left(\frac{\phi_{0,1} - \phi}{\sigma_{0,1}}\right)\right] + B_1 \left[1 + \tanh\left(\frac{\phi - \phi_{1,1}}{\sigma_{1,1}}\right)\right] + C_1 \left[1 + \tanh\left(\frac{\phi - \phi_{2,1}}{\sigma_{2,1}}\right)\right]} \quad (6)$$

$$f_2(\phi) = \frac{1}{2} \left[1 + \tanh\left(\frac{\phi_{0,2} - \phi}{\sigma_{0,2}}\right)\right] + \frac{B_2}{2} \left[1 + \tanh\left(\frac{\phi - \phi_{1,2}}{\sigma_{1,2}}\right)\right] + \frac{C_2}{2} \left[1 + \tanh\left(\frac{\phi - \phi_{2,2}}{\sigma_{2,2}}\right)\right] \times \left[1 + \tanh\left(\frac{\phi_{3,2} - \phi}{\sigma_{3,2}}\right)\right], \quad (7)$$

where the coefficients are summarized in Table 4.

To validate the 2S_CH4_BFER scheme, calculations of premixed laminar methane/air flames were performed using CANTERA [21] for three different values of fresh gas temperature ($T_f = 300, 500, 700\text{K}$) and pressure ($P = 1, 3, 10 \text{ atm}$). Ten equivalence ratios have been tested, from $\phi = 0.6$ to $\phi = 1.5$. For the whole range of pressure and fresh gas temperature, the 2S_CH4_BFER scheme reproduces well the laminar flame speed in comparison with the GRI 3.0 mechanism (Fig. 3). The largest discrepancies occur for $T_f = 300 \text{ K}, P = 10 \text{ atm}$ (up to 32%) and $T_f = 700 \text{ K}, P = 3 \text{ atm}$ (up to 19%) due to the variations of the pressure dependency coefficient observed at these conditions. The temperature dependency is well preserved. Focusing on the Preccinsta case, the results at ambient pressure and temperature are very close to the GRI 3.0 mechanism. In Fig. 4, the adiabatic temperature

obtained at $T_f = 300\text{ K}$ and $P = 1\text{ atm}$ with the 2S_CH4_BFER scheme is plotted versus equivalence ratio and compared to equilibrium values using the 6 species involved in the reduced scheme and the 53 species involved in the GRI 3.0 mechanism. The agreement is very good up to $\phi = 1.4$, as expected when using two-step chemical schemes [18]. This shows also that the scheme should perform well in the Preccinsta burner where experiments indicate that the local equivalence ratio in the chamber never exceeds $\phi = 1.4$ ($z \simeq 0.08$ in Fig. 2).

2.2 *The numerical setup*

A compressible LES code [4,12,22–32] is used to solve the Navier-Stokes equations on hybrid (structured and unstructured) grids with real thermochemistry. A Taylor-Galerkin weighted residual central distribution scheme is used for the numerical integration [28,33,34]. It is a finite element based scheme, providing third-order accuracy in time and space on unstructured meshes. The interaction between chemical kinetics and turbulence is modeled by the Dynamically Thickened Flame (TFLES) model [22].

The computational domain (Fig. 5) extends downstream of the combustion chamber to take into account a part of the outside atmosphere. The full geometry is meshed including the twelve holes located upstream of the swirler. The mesh shown in Fig. 6 is unstructured and contains five million tetrahedral elements. It is refined inside the swirler vanes to capture mixing. There are at least five cells in the radial direction of each methane injection hole, which means that the characteristic cell length is about 0.2 mm in this

region. Those cells are the smallest of the computational domain. The characteristic size of the cells where reactions take place is about 1 *mm*: a local thickening factor of ten is sufficient to obtain at least five points in the flame front.

The inlets (air and fuel) and the outlet are described by Navier-Stokes Characteristic Boundary Conditions (NSCBC) [35,28,36]. An adiabatic no-slip condition is applied for all walls. All simulations are performed on the same mesh and with the same numerical parameters: only the boundary condition specifications vary. If the perfect mixing assumption is applied (cases A and C), the fuel injection holes are considered as walls and a perfectly premixed methane/air mixture is injected at the plenum inlet (the composition of the mixture varies accordingly to the equivalence ratio analyzed). Otherwise (cases B and D), dry air is imposed at the plenum inlet and pure methane at the swirler holes, as evidenced by an instantaneous iso-surface of CH_4 species mass fraction equal to 0.5 in Fig. 7. At the inlet of the plenum and the methane injections, mass flow is imposed (Table 2). Fresh gases are injected at 320 K for all simulations¹.

¹ In the experiments, the inlet fuel/air mixture temperature varies between 320 and 380 K. Moreover, the ambient pressure varies between 995 and 1030 mbar. These differences could have a moderate effect on the results.

3 Results and discussions

3.1 The 'quiet' flame - $\phi = 0.83$

At $\phi = 0.83$ (case 2a), the Preccinsta burner is experimentally characterized by a quiet flame stabilized at the nozzle exit. Two different numerical simulations have been performed for this operating point:

- **Case A:** Previous LES for this operating point [12–15] have correctly reproduced a quiet flame when injecting a perfectly premixed mixture at the inlet. Similar conclusions were reached here.
- **Case B:** In this case, methane and air are injected separately. Figure 8 compares the numerical correlation between temperature and mixture fraction to experimental results in the first section downstream of the nozzle exit ($h = 6 \text{ mm}$) for different radial positions. Light-grey samples are collected at $r = 13 - 16 \text{ mm}$ close to the injection of fresh gases into the chamber where the temperature is low and the mixture fraction variance is maximum. Even if the experimental extreme values of mixture fraction ($z_{min} \approx 0.03$ and $z_{max} \approx 0.07$) are not captured by LES, the mixture fraction distribution is correctly reproduced (Fig. 9). The reaction zone is roughly represented by the black symbols ($r = 8 - 12 \text{ mm}$) in Fig. 8: it is a region of intermittency between fresh and burnt gases. The charcoal-grey symbols in Fig. 8 correspond approximately to the IRZ. It is almost an equilibrium state: the temperature reaches the adiabatic value and the equivalence ratio is close to the mean value of the combustor ($\bar{z} = 0.0463$). Both the reaction zone and the IRZ are correctly reproduced by the simulation. Discrepancies between experimental and numerical results are mainly

detected in the Outer Recirculation Zone (ORZ) corresponding to $r = 18 - 30 \text{ mm}$ (mid-grey symbols): the temperature is overestimated most likely because heat losses at the chamber walls and radiation effects are not taken into account. Nevertheless, the flame structure is well characterized and the mixing between fresh air and methane is correctly described. Figure 10a. compares the scatterplots of computed temperature versus mixture fraction with the experimental results at three sections further in the combustion chamber ($h = 10, 30$ and 80 mm). As the distance from the swirler exit increases, the mixture fraction variations are reduced and the local gas state approaches equilibrium. Note that LES has some difficulties capturing the presence of fresh gases at $h = 15 \text{ mm}$ and predicts a slightly shorter flame. Nevertheless, the experimental mixture fraction distribution is correctly reproduced by the computations (Fig. 10b.).

Figure 11 compares the mean temperature profiles at eight different sections in the chamber obtained numerically with (case B) and without (case A) the perfect premixing hypothesis (line and dashed-line respectively) with the experimental results (symbols). The simulations correctly reproduce the IRZ and the reaction zone. The temperature in the ORZ is overestimated since wall heat losses and radiation effects are not taken into account. Mean profiles reveal no significant differences between the two LES. Figure 12 compares numerical and experimental temperature fluctuation profiles. When air and methane are injected separately, the flame oscillations are slightly increased and the temperature fluctuations are better described in the reaction zone. Nevertheless, the fluctuations within the ORZ and IRZ are still underestimated due to the adiabatic hypothesis. Mean and RMS profiles of CO_2 provide similar levels of agreement with experiments (Figs. 13–14). The

description of CO_2 fluctuations is slightly improved when injecting methane and air separately (case B) but no difference between the numerical results is detected in the mean profiles. For CO , the situation is different: Fig. 15 compares LES mean profiles of CO with experimental results for which error bars are introduced. Although both simulations greatly underestimate the levels of CO species, it is difficult to conclude since experimental results show an error bar of about 50%. All other species are correctly described and the quality of the results is similar to that of CO_2 (not shown).

3.2 The 'pulsating' flame - $\phi = 0.7$

The Preccinsta burner has never been computed for an equivalence ratio of $\phi = 0.7$, which corresponds to a 'pulsating' flame oscillating around its mean position located in the near field of the nozzle exit. Figure 16 displays the temporal evolution of heat release, mixture fraction and pressure fluctuations before the exit nozzle (probe I in Fig. 1) for the two numerical simulations performed at this operating point:

- **Case C:** Assuming perfect premixing, no variation of the mixture fraction is detected and oscillations of pressure are small at probe I . Heat release localizes the reaction zone and consequently, the flame position. In this case, it is constantly equal to zero: a quiet flame is stabilized at the nozzle in contrast with the experimental results.
- **Case D:** When methane and air are injected separately, higher pressure oscillations are observed before the nozzle exit (Fig. 16c.). High heat release fluctuations are detected at probe I (Fig. 16a.), which indicates a pulsating flame and supports the experimental observation that the fluctuations in

equivalence ratio at the nozzle are the cause of the thermo-acoustic instabilities.

LES and experiments are compared at the first section downstream of the nozzle exit ($h = 6 \text{ mm}$) in terms of correlation between temperature and mixture fraction (Fig. 17) and distribution of mixture fraction (Fig. 18). These figures can be compared to Figs. 8 and 9 respectively for the 'quiet' flame (case B): obviously, case D exhibits much higher unmixedness and temperature variations. The experimental distribution of mixture fraction is correctly reproduced even if the experimental extreme values of mixture fraction, $z_{min} \approx 0.015$ and $z_{max} \approx 0.08$ respectively, are not captured (Fig. 17). Within the chamber ($h = 10, 30$ and 80 mm), the scatterplots of temperature versus mixture fraction also match experimental results (Fig. 19a.) and the mixture fraction distribution is correctly estimated (Fig. 19b.).

The mean profiles obtained for case D correspond to a pulsating situation. Velocity has been measured for this case and LES profiles of the mean velocity-components (axial, radial and tangential) can be compared to LDV measurements at five sections downstream of the injector (Figs. 20, 21 and 22). Three different regions can be detected looking at the mean axial velocity: the injection of fresh gases generates a conically-shaped flow characterized by high positive axial and tangential velocity values; a reverse flow is detected in the IRZ and the ORZ is characterized by low velocities. Profiles are generally improved for case D: the opening of fresh gas injection is correctly captured and the negative velocity values that characterize the IRZ reach approximately 20 m/s at $h = 1.5 \text{ mm}$ as measured experimentally.

The mean temperature profiles for cases C and D are compared to the experimental results in Fig. 23. The agreement between numerical and experimental results is generally good. The temperature of the IRZ and the reaction region are better described by the non perfectly-premixed LES (case D). Again, temperature profiles are overestimated in the ORZ. The perfect premixing hypothesis (case C) has a strong effect on the temperature fluctuations (Fig. 24). Since LES for case C leads to a quiet flame and does not capture the instability, the temperature fluctuations are greatly underestimated, whereas case D correctly predicts them. This difference is more evident in the IRZ than in other regions and clearly shows the importance of computing mixing if the objective is to capture unstable modes.

Finally, the mean and RMS profiles of CO_2 (Figs. 25–26) lead to the same conclusions: mean CO_2 profiles are slightly improved when assuming non perfect premixing, but the RMS profiles are much better captured when the methane jets are calculated (case D). All other species profiles (not shown) confirm these results except CO for which experimental uncertainties are high.

Time evolutions of the fluctuations of total heat release q and chamber pressure p_C (probe C in Fig. 1) are shown in Fig 27 for case D. Heat release and pressure oscillate at the same frequency, suggesting that the instability in case D is fed by a flame/acoustics coupling. The associated flapping frequency is found equal to $f_{num} \approx 390 \text{ Hz}$ for case D, when the experimental value f_{exp} is close to 290 Hz . This discrepancy could be due to the acoustic impedance at the fuel injection which was not characterized experimentally and arbitrarily imposed in LES.

Despite this limitation, a phase-averaged description of LES dynamics is proposed in the following. For the analysis, the pressure drop ΔP (between probes P and C in Fig 1) and the pressure in the plenum P_P (probe P) are displayed in Fig. 28 for case D. As these two signals are almost in phase, the plenum pressure can be considered as a proper signal to perform phase-averaging analysis in the chamber. To compare with the experiments, numerical results are sampled at four phases of the pressure P_P over 20 cycles of the LES results: the minimum, maximum and medium values (reference points named as $ph1$, $ph5$, $ph3$ and $ph7$ in [11], see Fig. 28).

The feedback loop of the self-sustained pulsation can only be presumed in the experiments since no data is available for the swirler. But in LES, it can be visualized by displaying phase-locked instantaneous velocity fields (Fig. 29) and CH_4 fields (Fig. 30) of the 'pulsating' flame. When ΔP is small (phase $ph1$), the axial velocity in the swirler is low (Fig. 29). The methane jets are injected in a low velocity air stream. They are not deviated significantly and impact the wall of the chamber. Fuel accumulates in the swirler (phase $ph1$ in Fig. 30). At phase $ph3$, the air velocity is still low, the fuel mass fraction is maximum in the swirler and a lean mixture enters the chamber. When ΔP is maximum (phase $ph5$), the axial velocity within the swirler is high. The methane jets do not impact walls and the fuel accumulated in the swirler is pushed towards the chamber. It enters the chamber at phase $ph7$ (Fig. 30).

The time evolution of the axial velocity and mixture fraction near the exit nozzle (probe I in Fig. 1) together with the pressure drop are displayed in Fig. 31. LES supports experimental conclusions: the velocity field in the swirler oscillates when the pressure drop pulsates. This generates rich gas pockets that are cyclically pushed into the chamber [37]. A comparison of experimental and numerical phase locked images of mean CH_4 and temper-

ature in the chamber is provided in Fig. 32 for phases $ph1$, $ph3$, $ph5$ and $ph7$. The observation window is indicated by a dashed window in Fig. 1. It confirms that the fuel concentration at the swirler outlet is pulsating, leading to the observed temperature fluctuations. It also shows that LES captures this phenomenon correctly.

Conclusion

This study has provided a systematic comparison of mean and RMS fields obtained experimentally and by LES in the swirled methane/air combustor of Preccinsta (DLR). LES have been performed with a compressible solver to capture self-excited modes. Methane injection was either simplified by assuming perfect premixing upstream of the swirler or fully resolved by meshing all methane injectors and computing the mixing between air and methane within the swirler. Results demonstrate that assuming that the methane/air flow entering the chamber is perfectly premixed has a limited influence for the stable regime at $\phi = 0.83$: the mean and RMS fields obtained with or without perfect mixing assumptions are very close and agree well with experimental data. However, a strong effect of the perfect mixing assumption is observed on the unstable regime at $\phi = 0.7$: LES with perfectly premixed mixture remains stable while LES where the methane jets are resolved leads to a self-excited mode where the velocity pulsates and the fuel periodically accumulates within the swirler before entering the chamber and burning in a very unsteady mode. This result confirms the experimental study of Meier *et al.* [11] who indicated that insufficient mixing was probably the source of the unstable mode observed at $\phi = 0.7$.

The details of the exact mechanism controlling the instability mechanism itself were not identified yet but results demonstrate that both compressibility and methane/air mixing must be included in future codes trying to reproduce this type of unstable modes.

Acknowledgement

This research project has been supported by a Marie Curie Early Stage Research Training Fellowship of the European Communitys Sixth Framework Programme under contract number MEST-CT-2005-020426. This work was granted access to the HPC resources of CINES under the allocation 2010-025031 made by GENCI (Grand Equipement National de Calcul Intensif).

References

- [1] F. di Mare, W. Jones, K. Menzies, *Combust. Flame* 137 (2004) 278–294.
- [2] A. Sengissen, J. F. V. Kampen, R. Huls, G. Stoffels, J. B. W. Kok, T. Poinsot, *Combust. Flame* 150 (2007) 40–53.
- [3] M. Freitag, J. Janicka, *Proc. Combust. Inst.* 31 (2007) 1477–1485.
- [4] P. Schmitt, T. J. Poinsot, B. Schuermans, K. Geigle, *J. Fluid Mech.* 570 (2007) 17–46.
- [5] T. Lieuwen, V. Yang, *Combustion instabilities in gas turbine engines. operational experience, fundamental mechanisms and modeling*, in: *Prog. in Astronautics and Aeronautics AIAA*, Vol. 210, 2005.
- [6] T. Poinsot, D. Veynante, *Theoretical and Numerical Combustion*, R.T. Edwards, 2nd edition., 2005.
- [7] T. Lieuwen, H. Torres, C. Johnson, B. Zinn, *Journal of Engineering for Gas Turbines and Power* 123 (1) (2001) 182–189.
- [8] S. Sheekrishna, S. Hemchandra, T. Lieuwen, *Combust. Theory and Modelling* 14 (5) (2010) 681–714.
- [9] P. Weigand, X. Duan, W. Meier, U. Meier, M. Aigner, C. Bérat, *Experimental investigations of an oscillating lean premixed CH_4 /air swirl flame in a gas turbine model combustor*, in: *European Combustion Meeting*, 2005.
- [10] P. Weigand, W. Meier, X. Duan, M. Aigner, *Laser based investigations of thermo-acoustic instabilities in a lean premixed gas turbine model combustor*, in: *Proceedings of GT2006 ASME Turbo Expo 2006: Power for Land, Sea and Air*, Barcelona (Spain), May 8-11, 2007.

- [11] W. Meier, P. Weigand, X. Duan, R. Giezendanner-Thoben, *Combust. Flame* 150 (1-2) (2007) 2–26.
- [12] S. Roux, G. Lartigue, T. Poinsot, U. Meier, C. Bérat, *Combust. Flame* 141 (2005) 40–54.
- [13] J. Galpin, A. Naudin, L. Vervisch, C. Angelberger, O. Colin, P. Domingo, *Combust. Flame* 155 (1-2) (2008) 247–266.
- [14] B. Fiorina, R. Vicquelin, P. Auzillon, N. Darabiha, O. Gicquel, D. Veynante, *Combust. Flame* 157 (2010) 465–475.
- [15] V. Moureau, P. Domingo, L. Vervisch, *Combust. Flame* (2011) *in Press*.
- [16] G. Albouze, L. Gicquel, T. Poinsot, *Comptes Rendus Mécanique* 337 (2009) 318–328.
- [17] R. W. Bilger, B. Yip, M. B. Long, A. R. Masri, *Combust. Sci. Tech.* 72 (4-6) (1990) 137–155.
- [18] B. Franzelli, E. Riber, M. Sanjosé, T. Poinsot, *Combust. Flame* 157 (7) (2010) 1364–1373.
- [19] F. Frenklach, H. Wang, C.-L. Yu, M. Goldenberg, C. Bowman, R. Hanson, D. Davidson, E. Chang, G. Smith, D. Golden, W. Gardiner, V. Lissianski, http://www.me.berkeley.edu/gri_mech.
- [20] C. Westbrook, F.L. Dryer, *Combust. Flame* 37 (1980) 171–192.
- [21] D.G. Goodwin, *Cantera C++ Users Guide*, <http://sourceforge.net/projects/cantera> (2002).
- [22] O. Colin, F. Ducros, D. Veynante, T. Poinsot, *Phys. Fluids* 12 (7) (2000) 1843–1863.
- [23] A. Kaufmann, F. Nicoud, T. Poinsot, *Combust. Flame* 131 (2002) 371–385.

- [24] L. Selle, G. Lartigue, T. Poinso, R. Koch, K.-U. Schildmacher, W. Krebs, B. Prade, P. Kaufmann, D. Veynante, *Combust. Flame* 137 (4) (2004) 489–505.
- [25] Y. Sommerer, D. Galley, T. Poinso, S. Ducruix, F. Lacas, D. Veynante, *J. Turb.* 5.
- [26] A. Roux, L. Y. M. Gicquel, Y. Sommerer, T. J. Poinso, *Combust. Flame* 152 (1-2) (2007) 154–176.
- [27] A. Giauque, L. Selle, T. Poinso, H. Buechner, P. Kaufmann, W. Krebs, *J. Turb.* 6 (21) (2005) 1–20.
- [28] V. Moureau, G. Lartigue, Y. Sommerer, C. Angelberger, O. Colin, T. Poinso, *J. Comput. Phys.* 202 (2) (2005) 710–736.
- [29] K. Truffin, T. Poinso, *Combust. Flame* 142 (4) (2005) 388–400.
- [30] L. Selle, L. Benoit, T. Poinso, F. Nicoud, W. Krebs, *Combust. Flame* 145 (1-2) (2006) 194–205.
- [31] G. Boudier, L. Y. M. Gicquel, T. Poinso, D. Bissières, C. Bérat, *Proc. Combust. Inst.* 31 (2007) 3075–3082.
- [32] A. Sengissen, A. Giauque, G. Staffelbach, M. Porta, W. Krebs, P. Kaufmann, T. Poinso, *Proc. Combust. Inst.* 31 (2007) 1729–1736.
- [33] O. Colin, *Simulations aux grandes échelles de la combustion turbulente prémélangée dans les statoréacteurs*, Phd thesis, INP Toulouse (2000).
- [34] O. Colin, M. Rudgyard, *J. Comput. Phys.* 162 (2) (2000) 338–371.
- [35] T. Poinso, S. Lele, *J. Comput. Phys.* 101 (1) (1992) 104–129.
- [36] V. Granet, O. Vermorel, T. Leonard, L. Gicquel, , T. Poinso, *Am. Inst. Aeronaut. Astronaut. J.* 48 (10) (2010) 2348–2364.

[37] P. Wolf, G. Staffelbach, A. Roux, L. Gicquel, T. Poinso, V. Moureau, C. R. Acad. Sci. Mécanique 337 (6-7) (2009) 385–394.

List of Tables

1	Flame parameters of the experimental cases. The mixture fraction is based on the Bilger [17] definition.	26
2	Numerical cases.	26
3	Activation energy E_a , pre-exponential factor A , and reaction exponents n_k used for the <i>2S_CH4_BFER</i> mechanism. Units are: mol, s, cm ³ and cal/mol.	27
4	Coefficients for the two correction functions f_1 and f_2 in the <i>2S_CH4_BFER</i> scheme.	27

Tables

Table 1

Flame parameters of the experimental cases. The mixture fraction is based on the Bilger [17] definition.

Experimental case	1	2a	2b
Air flow rate [<i>g/min</i>]	734.2	734.2	734.2
Methane flow rate [<i>g/min</i>]	30.0	35.9	32.3
Thermal power [<i>kW</i>]	25.1	30.0	27.0
Equivalence ratio [-]	0.70	0.83	0.75
Mixture fraction [-]	0.0391	0.0463	0.0418

Table 2

Numerical cases.

Numerical case	A	B	C	D
Corresponding experimental case	2a	2a	1	1
Mixing	Perfect	Non-perfect	Perfect	Non-perfect
Equivalence ratio [-]	0.83	0.83	0.7	0.7
Plenum composition	Air+CH ₄	Air	Air+CH ₄	Air
Plenum flow rate [<i>g/min</i>]	734.2	734.2	734.2	734.2
Holes composition	-	CH ₄	-	CH ₄
Holes flow rate [<i>g/min</i>]	-	35.9	-	30.0

Table 3

Activation energy E_a , pre-exponential factor A , and reaction exponents n_k used for the 2S-CH₄-BFER mechanism. Units are: mol, s, cm³ and cal/mol.

	CH ₄ oxidation		CO-CO ₂ equilibrium	
Activation energy	3.55×10^4		1.2×10^4	
Temperature exponent	0.0		0.8	
Pre-exponential factor	4.9×10^9		2×10^8	
Reaction exponents (-)	n_{CH_4}	0.50	n_{CO}	1.00
	$n_{O_2,1}$	0.65	$n_{O_2,2}$	0.50

Table 4

Coefficients for the two correction functions f_1 and f_2 in the 2S-CH₄-BFER scheme.

	$\phi_{0,j}$	$\sigma_{0,j}$	B_j	$\phi_{1,j}$	$\sigma_{1,j}$	C_j	$\phi_{2,j}$	$\sigma_{2,j}$	$\phi_{3,j}$	$\sigma_{3,j}$
$j = 1$	1.1	0.09	0.37	1.13	0.03	6.7	1.6	0.22	-	-
$j = 2$	0.95	0.08	$2.5 \cdot 10^{-5}$	1.3	0.04	0.0087	1.2	0.04	1.2	0.05

List of Figures

- 1 Schematic of the Preccinsta design. Probe P is located in the plenum at $h = -70 \text{ mm}$. Probe I is located in the injector before the swirler exit ($h = -5 \text{ mm}$) and probe C is in the chamber at $h = 10 \text{ mm}$. 34
- 2 Correlation between temperature and mixture fraction at section $h = 6 \text{ mm}$ for a., the 'quiet' flame (case 2a in Table 1) and b., the 'pulsating' flame (case1). Symbols represent single-shot Raman measurements at different radial positions. The solid line shows the equilibrium temperature whereas the vertical dashed line indicates the global mixture fraction (experimental data from [11]). 34
- 3 Laminar flame speed versus equivalence ratio at fresh gas temperature $T_f = 300\text{K}$ (a.), 500K (b.) and 700K (c.). Comparison between 2S_CH4_BFER scheme (solid lines) and GRI 3.0 detailed mechanism (symbols) for pressure $P = 1, 3, 10 \text{ atm}$. 35
- 4 Burnt gas temperature versus equivalence ratio. Comparison between GRI3.0 mechanism (—), equilibrium results (\times) and 2S_CH4_BFER scheme (\circ) at pressure $P = 1 \text{ atm}$ and fresh gas temperature $T_f = 300 \text{ K}$. 36
- 5 Schematic of the computational domain. 37
- 6 Computational half-domain mesh. 37

- 7 Detail of the twelve computational holes upstream of the swirler for the methane injection (LES's numerical cases B and D in Table 2). Instantaneous iso-surface of methane mass fraction equal to 0.5. 38
- 8 Correlation between temperature and mixture fraction for the 'quiet' flame ($\phi = 0.83$) at $h = 6 \text{ mm}$. Comparison between a., experiments (case 2a) and b., simulations (case B). 38
- 9 Experimental (case 2a - solid line) and numerical (case B - dashed line) mixture fraction distribution at $h = 6 \text{ mm}$ for the 'quiet' flame ($\phi = 0.83$). The global mixture fraction is indicated by the vertical line. 39
- 10 a. Experimental (case 2a) and numerical (case B) correlation between temperature and mixture fraction for the 'quiet' flame ($\phi = 0.83$) at $h = 15, 30$ and 80 mm . b. Experimental (case 2a - solid line) and numerical (case B - dashed line) distribution of the mixture fraction at $h = 15, 30$ and 80 mm for the 'quiet' flame. 40
- 11 Mean temperature profiles for the 'quiet' flame ($\phi = 0.83$) at eight sections in the chamber. The experimental results (symbols) are compared to numerical results: perfectly premixed simulation (case A - solid line) and non perfectly premixed simulation (case B - dashed line). 41

- 12 RMS temperature profiles for the 'quiet' flame ($\phi = 0.83$) at eight sections in the chamber. The experimental results (symbols) are compared to numerical results: perfectly premixed simulation (case A - solid line) and non perfectly premixed simulation (case B - dashed line). 42
- 13 Mean CO_2 species profiles for the 'quiet' flame ($\phi = 0.83$) at eight sections in the chamber. The experimental results (symbols) are compared to numerical results: perfectly premixed simulation (case A - solid line) and non perfectly premixed simulation (case B - dashed line). 43
- 14 RMS CO_2 species profiles for the 'quiet' flame ($\phi = 0.83$) at eight sections in the chamber. The experimental results (symbols) are compared to numerical results: perfectly premixed simulation (case A - solid line) and non perfectly premixed simulation (case B - dashed line). 44
- 15 Mean CO species profiles for the 'quiet' flame ($\phi = 0.83$) at eight sections in the chamber. The experimental results (symbols) are compared to numerical results: perfectly premixed simulation (case A - solid line) and non perfectly premixed simulation (case B - dashed line). 45
- 16 Temporal evolution of the heat release (a.), mixture fraction (b.) and pressure (c.) at probe I for the 'pulsating' flame ($\phi = 0.7$). Comparison between perfectly premixed simulation (case C - solid line) and the non perfectly premixed simulation (case D - dashed line). 46

- 17 Correlation between temperature and mixture fraction for the 'pulsating' flame ($\phi = 0.7$) at $h = 6 \text{ mm}$. Comparison between a., experimental (case 1) and b., numerical results (case D). 47
- 18 Experimental (case 1 - solid line) and numerical (case D - dashed line) distribution of mixture fraction at $h = 6 \text{ mm}$ for the 'pulsating' flame ($\phi = 0.7$). The global mixture fraction is indicated by the vertical line. 48
- 19 a. Experimental (case 1) and numerical (case D) correlation between temperature and mixture fraction for the 'pulsating' flame ($\phi = 0.7$) at $h = 15, 30$ and 80 mm . b) Experimental (case 1 - solid line) and numerical (case D - dashed line) distribution of mixture fraction at $h = 15, 30$ and 80 mm for the 'pulsating' flame. 49
- 20 Mean axial velocity profiles for the 'pulsating' flame ($\phi = 0.7$) at five sections in the chamber. The experimental results (symbols) are compared to numerical results: perfectly premixed simulation (case C - solid line) and non perfectly premixed simulation (case D - dashed line). 50
- 21 Mean radial velocity profiles for the 'pulsating' flame ($\phi = 0.7$) at five sections in the chamber. The experimental results (symbols) are compared to numerical results: perfectly premixed simulation (case C - solid line) and non perfectly premixed simulation (case D - dashed line). 51

- 22 Mean tangential velocity profiles for the 'pulsating' flame ($\phi = 0.7$) at five sections in the chamber. The experimental results (symbols) are compared to numerical results: perfectly premixed simulation (case C - solid line) and non perfectly premixed simulation (case D - dashed line). 52
- 23 Mean temperature profiles for the 'pulsating' flame ($\phi = 0.7$) at eight sections in the chamber. The experimental results (symbols) are compared to numerical data: perfect premixed (case C - solid line) and non perfect premixed simulation (case D - dashed line). 53
- 24 RMS temperature profiles for the 'pulsating' flame ($\phi = 0.7$) at eight sections in the chamber. The experimental results (symbols) are compared to numerical data: perfect premixed (case C - solid line) and non perfect premixed simulation (case D - dashed line). 54
- 25 Mean CO_2 profiles for the 'pulsating' flame ($\phi = 0.7$) at eight sections in the chamber. The experimental results (symbols) are compared to numerical data: perfect premixed (case C - solid line) and non perfect premixed simulation (case D - dashed line). 55
- 26 RMS CO_2 profiles for the 'pulsating' flame ($\phi = 0.7$) at eight sections in the chamber. The experimental results (symbols) are compared to numerical data: perfect premixed (case C - solid line) and non perfect premixed simulation (case D - dashed line). 56

- 27 Temporal evolution of the fluctuations of chamber pressure p_C (solid line, probe C in Fig. 1) and total heat release q (dashed line) for the 'pulsating' flame (case D). 57
- 28 Temporal evolution of the plenum pressure P_P at probe P in Fig. 1 (solid line) and the pressure drop ΔP (dashed line) between plenum and chamber (probe C in Fig. 1) for the 'pulsating' flame (case D). 58
- 29 Phase-locked instantaneous axial velocity fields for four different phases $ph1$, $ph2$, $ph3$ and $ph4$ for the 'pulsating' flame ($\phi = 0.7$, case D). 59
- 30 Phase-locked instantaneous CH_4 mass fraction fields for four different phases $ph1$, $ph2$, $ph3$ and $ph4$ for the 'pulsating' flame ($\phi = 0.7$, case D). 60
- 31 Temporal evolution of the pressure drop (solid line), axial velocity (dashed line) and mixture fraction (dotted-dashed line) in the swirler (probe I) for the 'pulsating' flame ($\phi = 0.7$, case D). 61
- 32 Phase-locked mean fields of CH_4 mass fraction (a.) and temperature (b.) in the chamber (visualization window displayed in Fig. 1, dashed line). Comparison between experiments (left, case1) and numerical simulation (right, case D) for the 'pulsating' flame ($\phi = 0.7$). 62

Figures

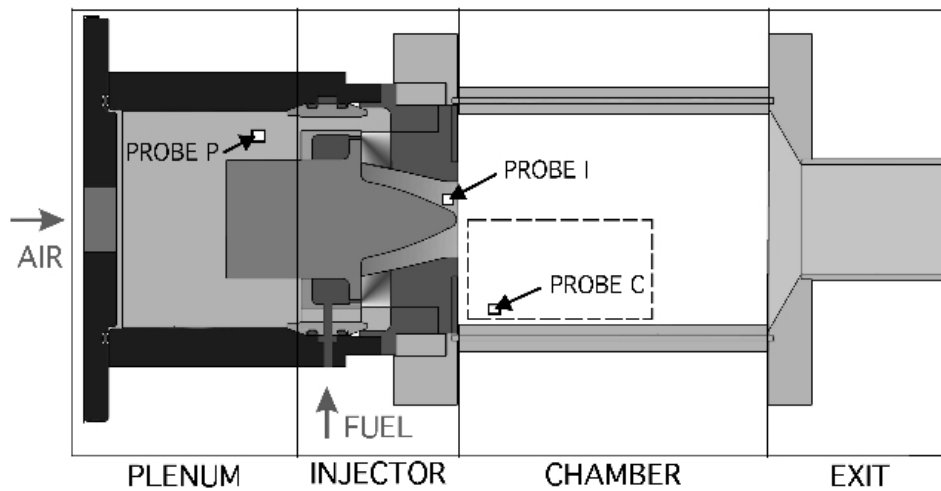


Fig. 1. Schematic of the Preccinsta design. Probe *P* is located in the plenum at $h = -70 \text{ mm}$. Probe *I* is located in the injector before the swirler exit ($h = -5 \text{ mm}$) and probe *C* is in the chamber at $h = 10 \text{ mm}$.

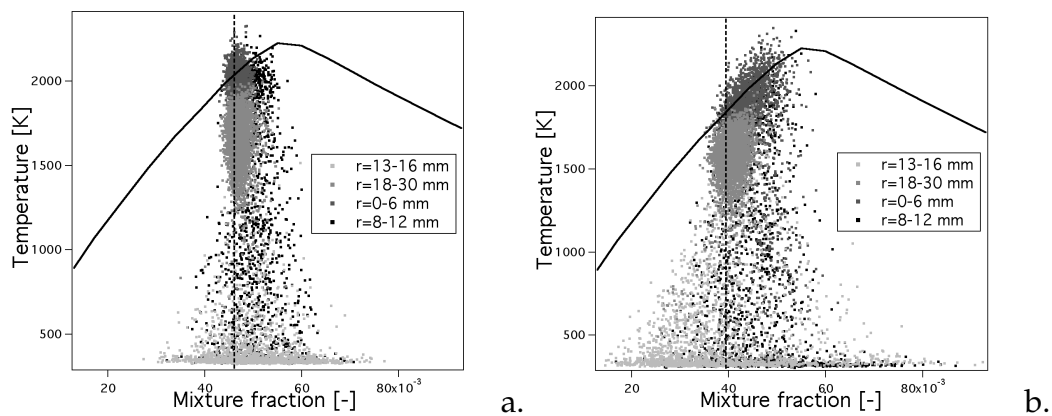


Fig. 2. Correlation between temperature and mixture fraction at section $h = 6 \text{ mm}$ for a., the 'quiet' flame (case 2a in Table 1) and b., the 'pulsating' flame (case1). Symbols represent single-shot Raman measurements at different radial positions. The solid line shows the equilibrium temperature whereas the vertical dashed line indicates the global mixture fraction (experimental data from [11]).

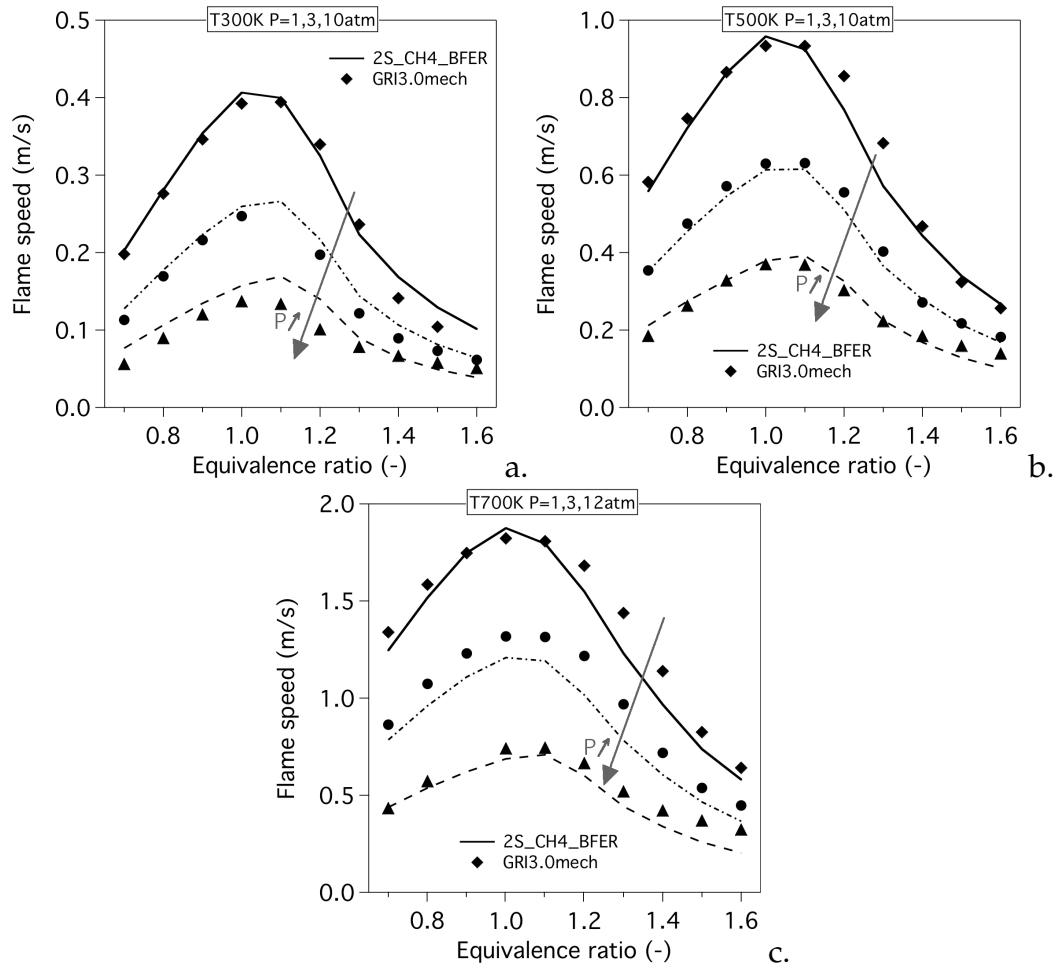


Fig. 3. Laminar flame speed versus equivalence ratio at fresh gas temperature $T_f = 300\text{K}$ (a.), 500K (b.) and 700K (c.). Comparison between 2S.CH4.BFER scheme (solid lines) and GRI 3.0 detailed mechanism (symbols) for pressure $P = 1, 3, 10\text{ atm}$.

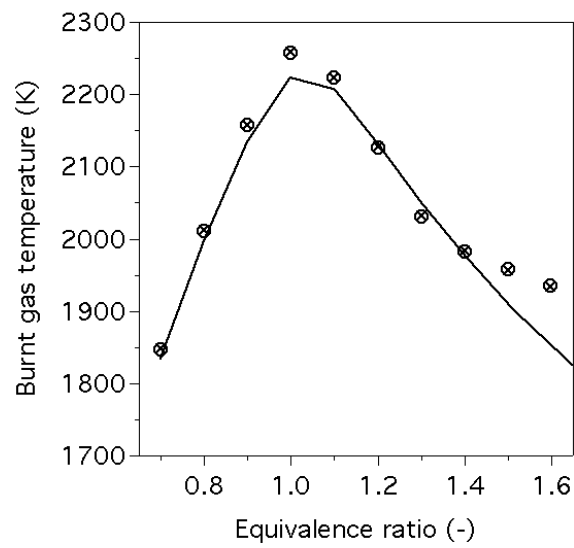


Fig. 4. Burnt gas temperature versus equivalence ratio. Comparison between GRI3.0 mechanism (—), equilibrium results (x) and 2S.CH4.BFER scheme (o) at pressure $P = 1 \text{ atm}$ and fresh gas temperature $T_f = 300 \text{ K}$.

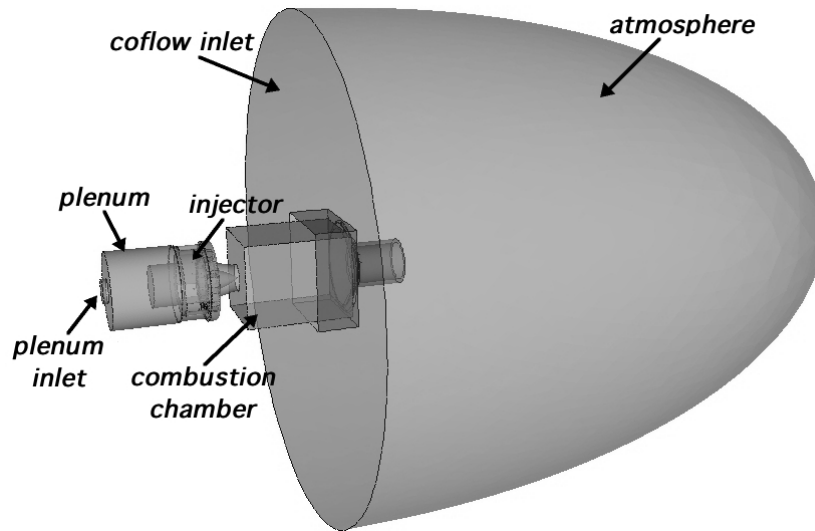


Fig. 5. Schematic of the computational domain.

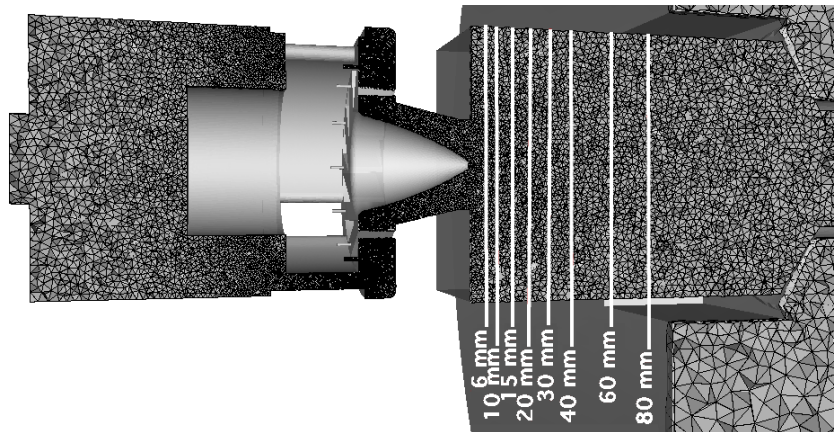


Fig. 6. Computational half-domain mesh.

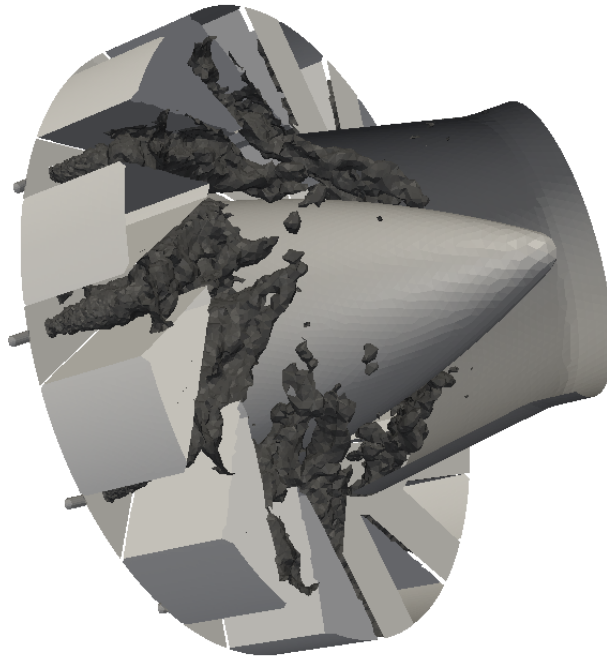


Fig. 7. Detail of the twelve computational holes upstream of the swirler for the methane injection (LES's numerical cases B and D in Table 2). Instantaneous iso-surface of methane mass fraction equal to 0.5.

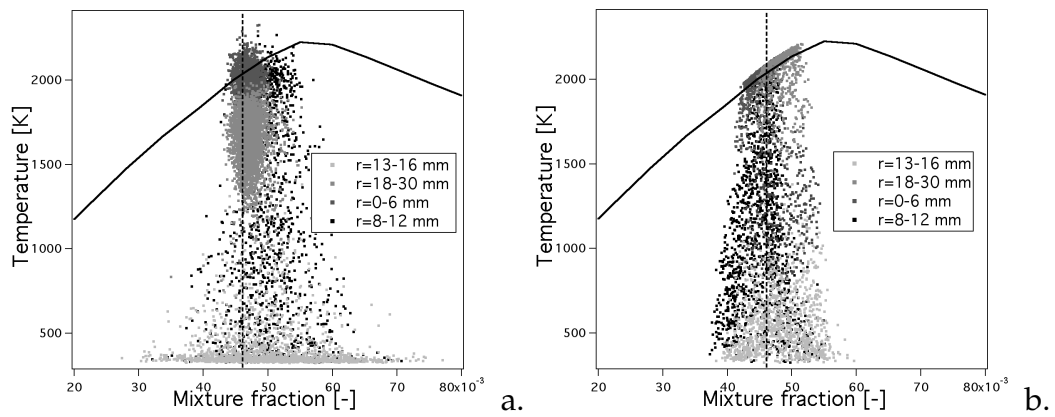


Fig. 8. Correlation between temperature and mixture fraction for the 'quiet' flame ($\phi = 0.83$) at $h = 6 \text{ mm}$. Comparison between a., experiments (case 2a) and b., simulations (case B).

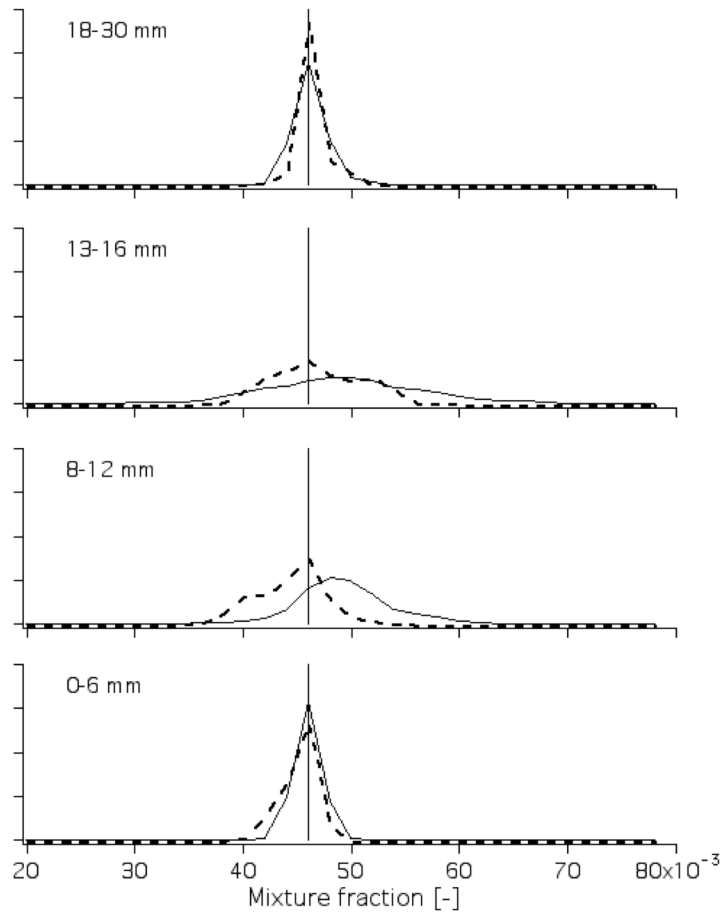


Fig. 9. Experimental (case 2a - solid line) and numerical (case B - dashed line) mixture fraction distribution at $h = 6 \text{ mm}$ for the 'quiet' flame ($\phi = 0.83$). The global mixture fraction is indicated by the vertical line.

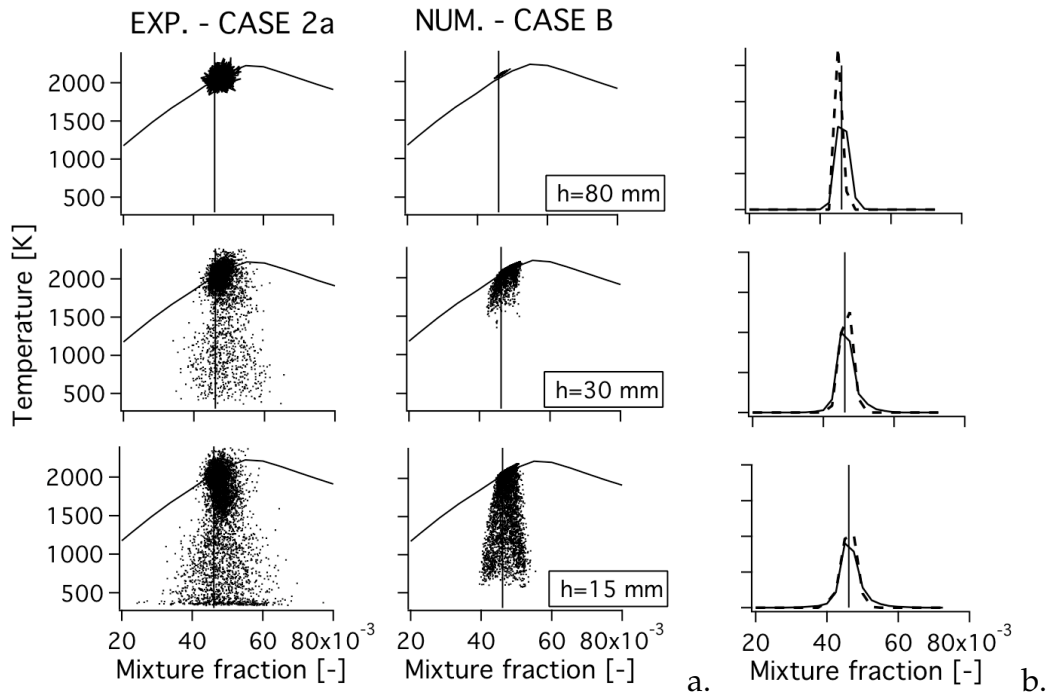


Fig. 10. a. Experimental (case 2a) and numerical (case B) correlation between temperature and mixture fraction for the 'quiet' flame ($\phi = 0.83$) at $h = 15, 30$ and 80 mm . b. Experimental (case 2a - solid line) and numerical (case B - dashed line) distribution of the mixture fraction at $h = 15, 30$ and 80 mm for the 'quiet' flame.

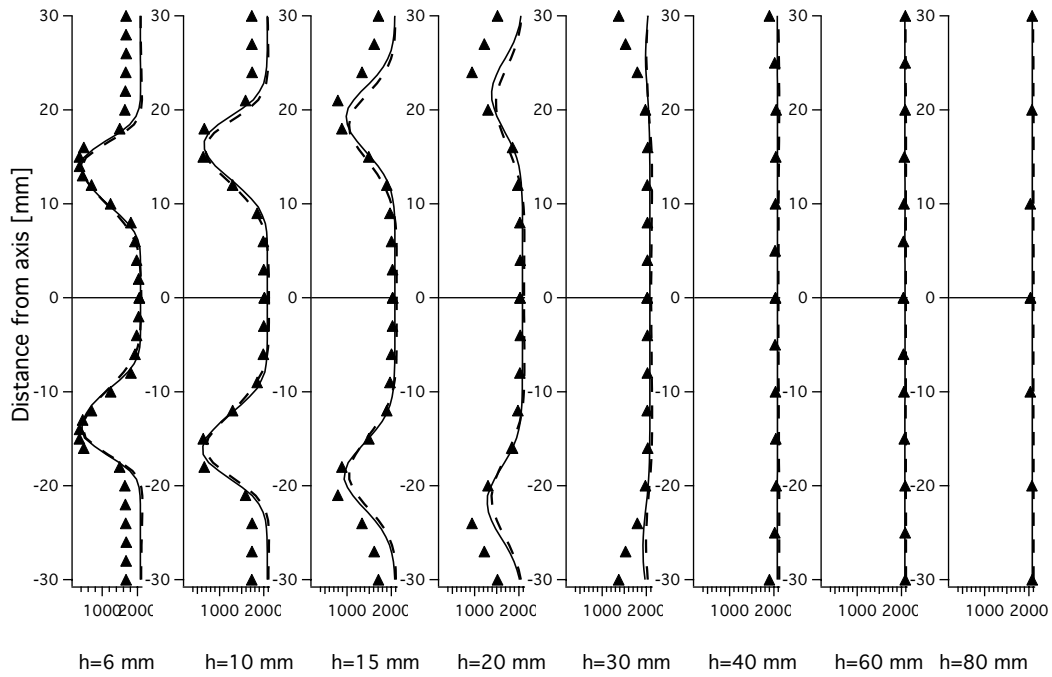


Fig. 11. Mean temperature profiles for the 'quiet' flame ($\phi = 0.83$) at eight sections in the chamber. The experimental results (symbols) are compared to numerical results: perfectly premixed simulation (case A - solid line) and non perfectly premixed simulation (case B - dashed line).

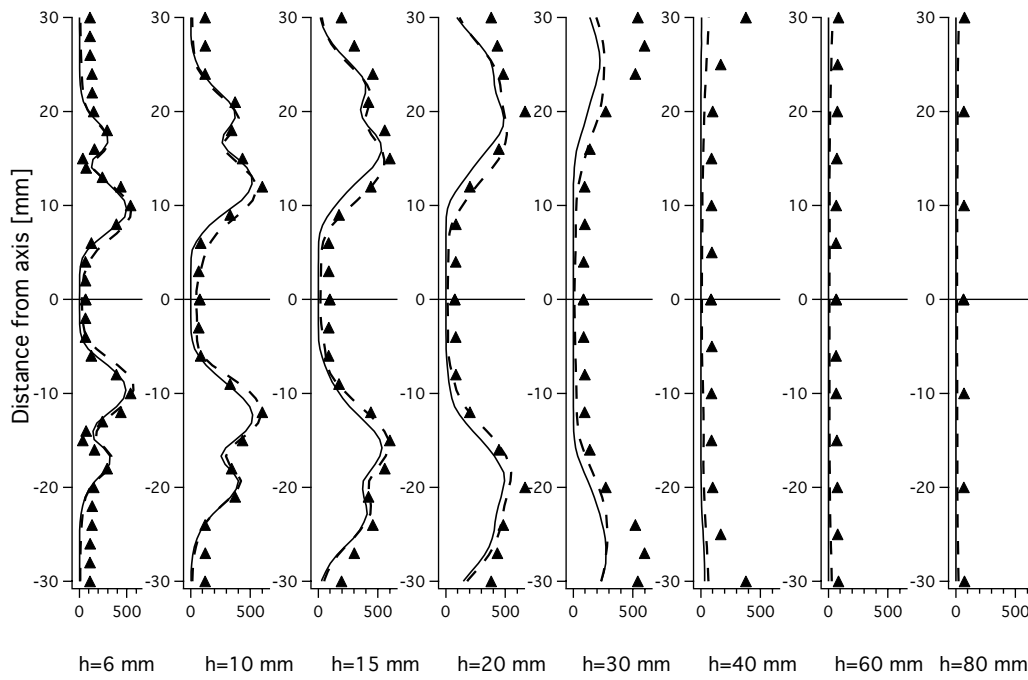


Fig. 12. RMS temperature profiles for the 'quiet' flame ($\phi = 0.83$) at eight sections in the chamber. The experimental results (symbols) are compared to numerical results: perfectly premixed simulation (case A - solid line) and non perfectly premixed simulation (case B - dashed line).

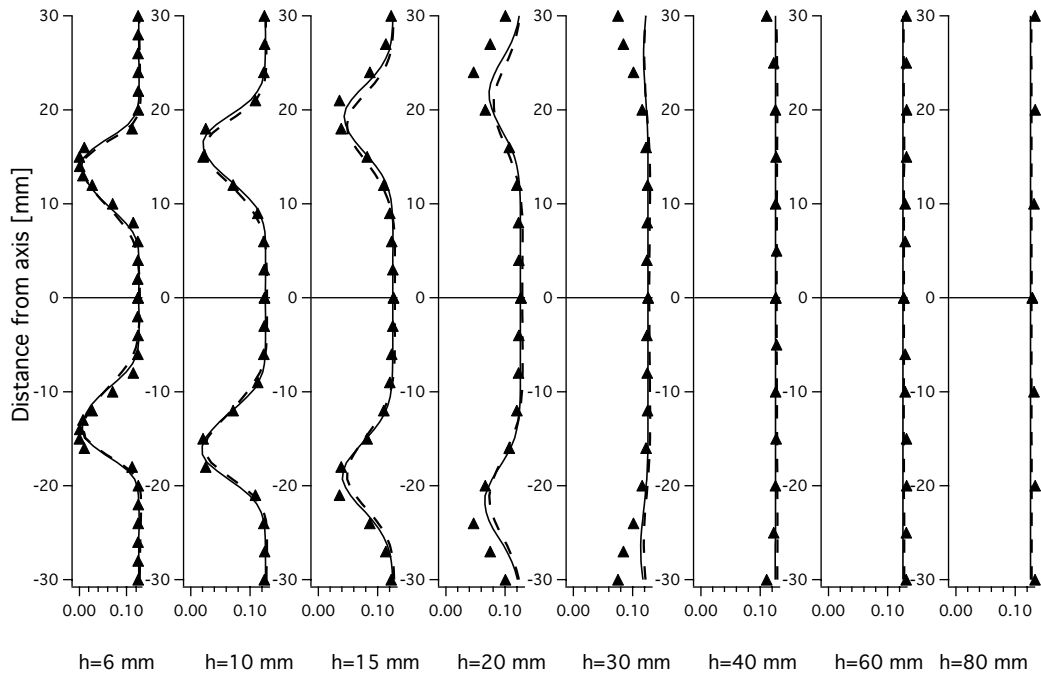


Fig. 13. Mean CO_2 species profiles for the 'quiet' flame ($\phi = 0.83$) at eight sections in the chamber. The experimental results (symbols) are compared to numerical results: perfectly premixed simulation (case A - solid line) and non perfectly premixed simulation (case B - dashed line).

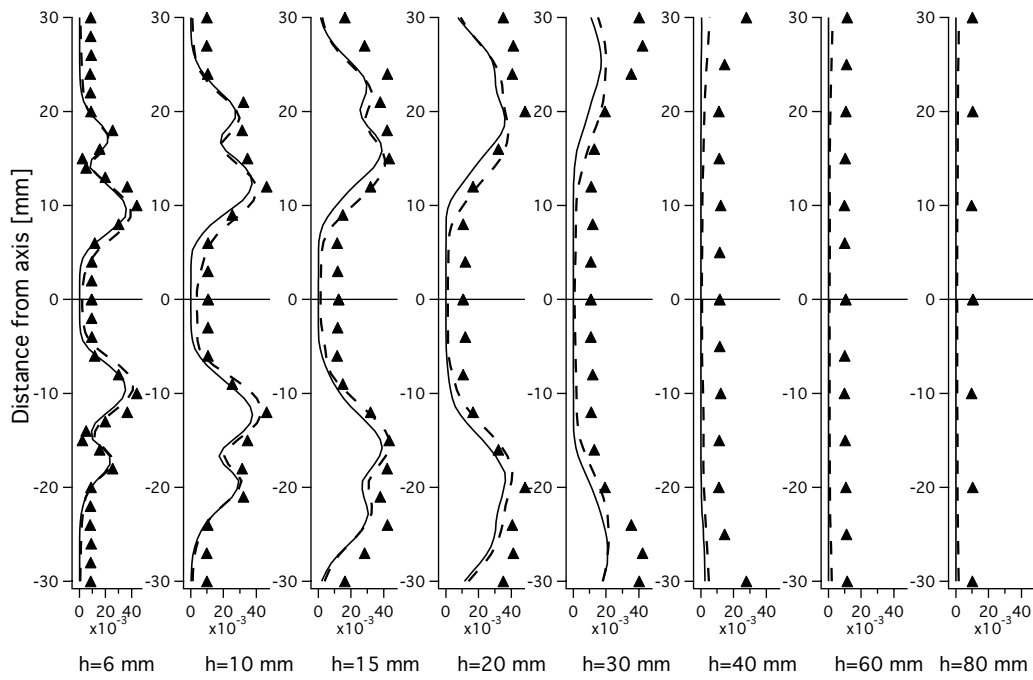


Fig. 14. RMS CO_2 species profiles for the 'quiet' flame ($\phi = 0.83$) at eight sections in the chamber. The experimental results (symbols) are compared to numerical results: perfectly premixed simulation (case A - solid line) and non perfectly premixed simulation (case B - dashed line).

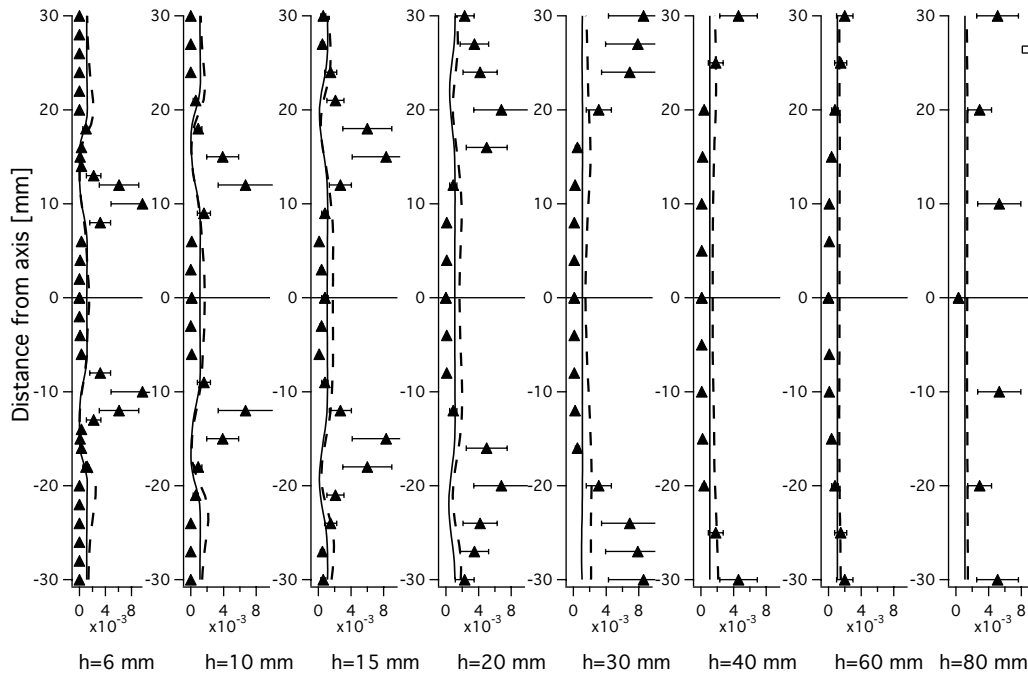


Fig. 15. Mean CO species profiles for the 'quiet' flame ($\phi = 0.83$) at eight sections in the chamber. The experimental results (symbols) are compared to numerical results: perfectly premixed simulation (case A - solid line) and non perfectly premixed simulation (case B - dashed line).

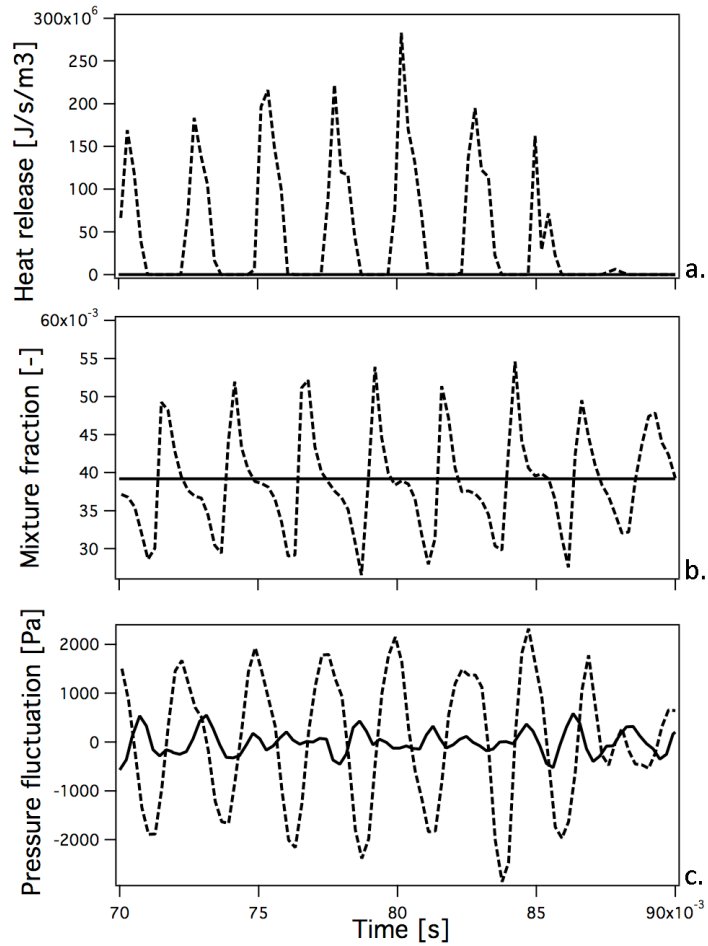


Fig. 16. Temporal evolution of the heat release (a.), mixture fraction (b.) and pressure (c.) at probe *I* for the 'pulsating' flame ($\phi = 0.7$). Comparison between perfectly premixed simulation (case C - solid line) and the non perfectly premixed simulation (case D - dashed line).

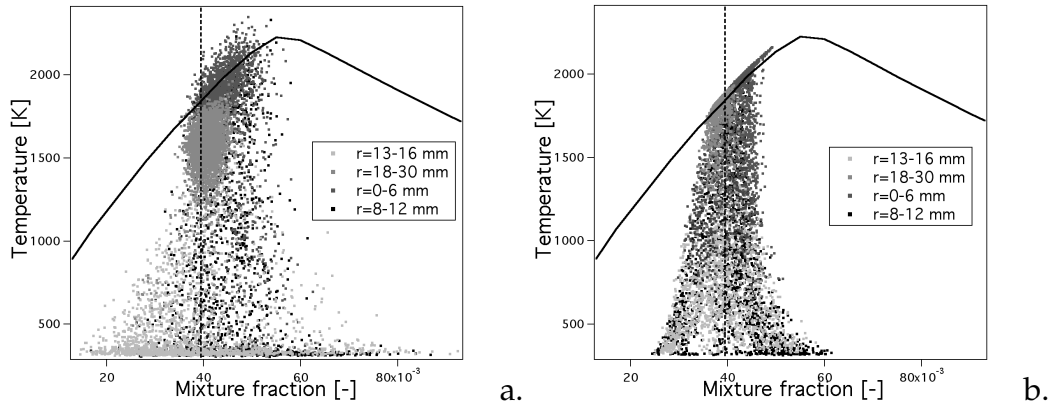


Fig. 17. Correlation between temperature and mixture fraction for the 'pulsating' flame ($\phi = 0.7$) at $h = 6 \text{ mm}$. Comparison between a., experimental (case 1) and b., numerical results (case D).

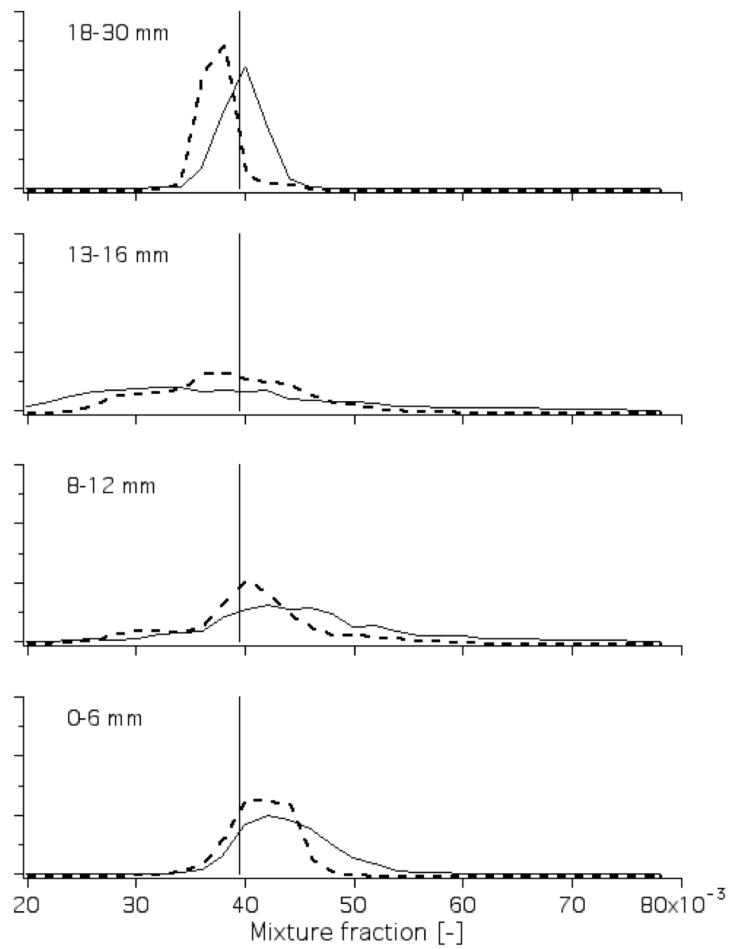


Fig. 18. Experimental (case 1 - solid line) and numerical (case D - dashed line) distribution of mixture fraction at $h = 6 \text{ mm}$ for the 'pulsating' flame ($\phi = 0.7$). The global mixture fraction is indicated by the vertical line.

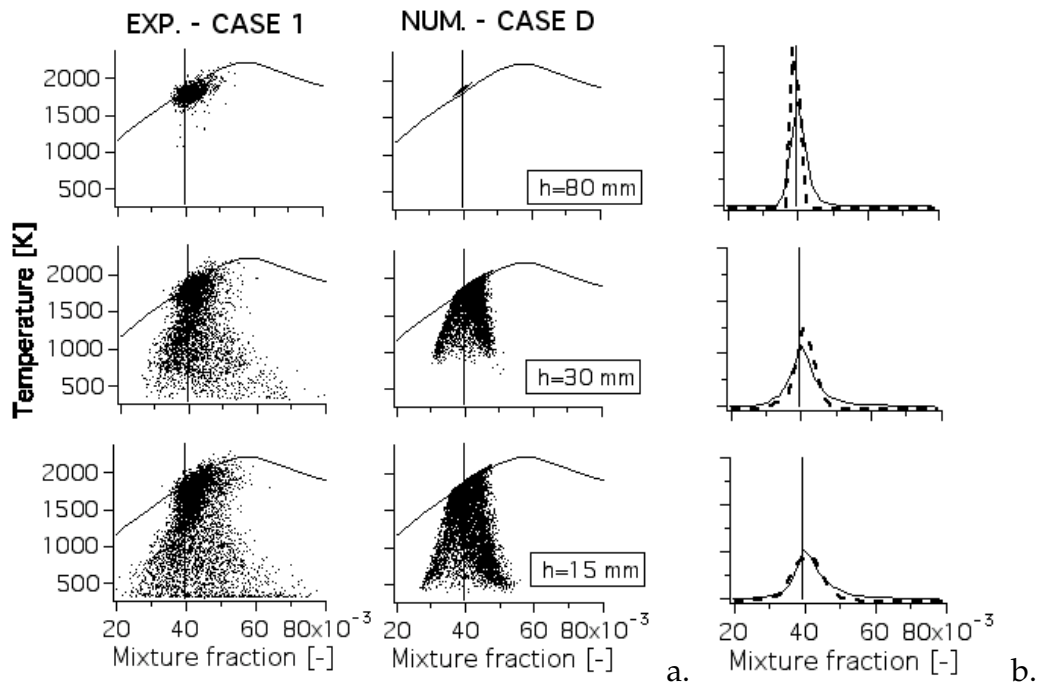


Fig. 19. a. Experimental (case 1) and numerical (case D) correlation between temperature and mixture fraction for the 'pulsating' flame ($\phi = 0.7$) at $h = 15, 30$ and 80 mm . b) Experimental (case 1 - solid line) and numerical (case D - dashed line) distribution of mixture fraction at $h = 15, 30$ and 80 mm for the 'pulsating' flame.

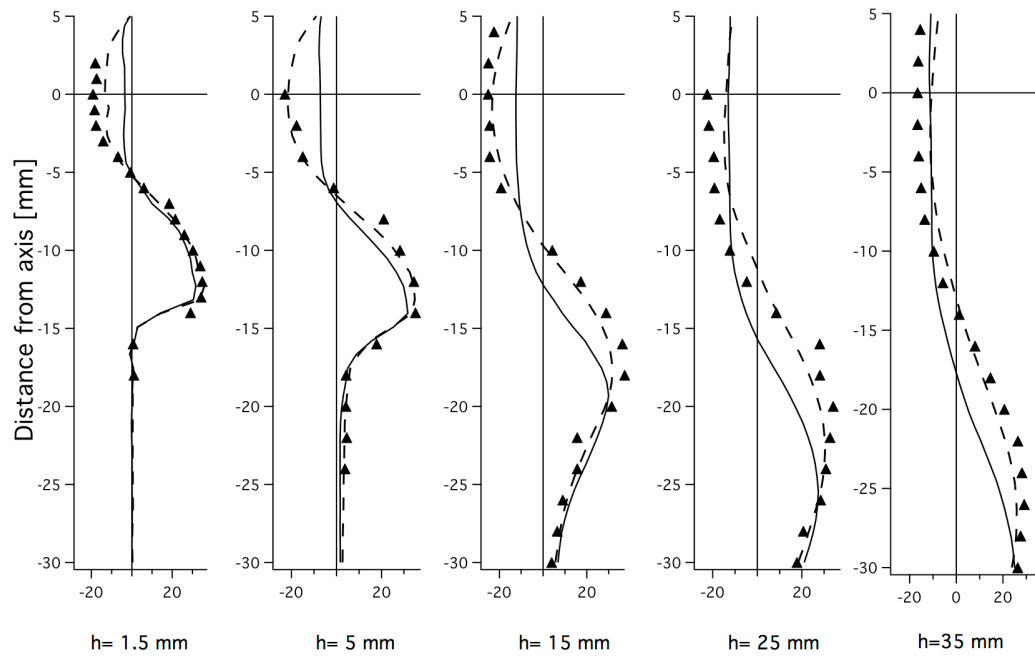


Fig. 20. Mean axial velocity profiles for the 'pulsating' flame ($\phi = 0.7$) at five sections in the chamber. The experimental results (symbols) are compared to numerical results: perfectly premixed simulation (case C - solid line) and non perfectly premixed simulation (case D - dashed line).

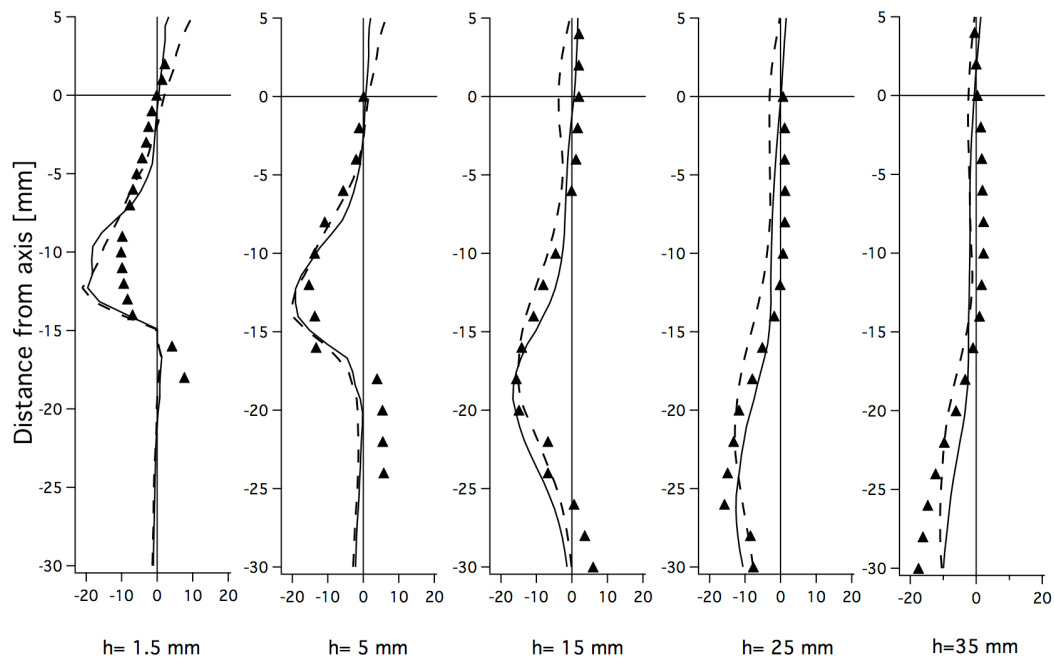


Fig. 21. Mean radial velocity profiles for the 'pulsating' flame ($\phi = 0.7$) at five sections in the chamber. The experimental results (symbols) are compared to numerical results: perfectly premixed simulation (case C - solid line) and non perfectly premixed simulation (case D - dashed line).

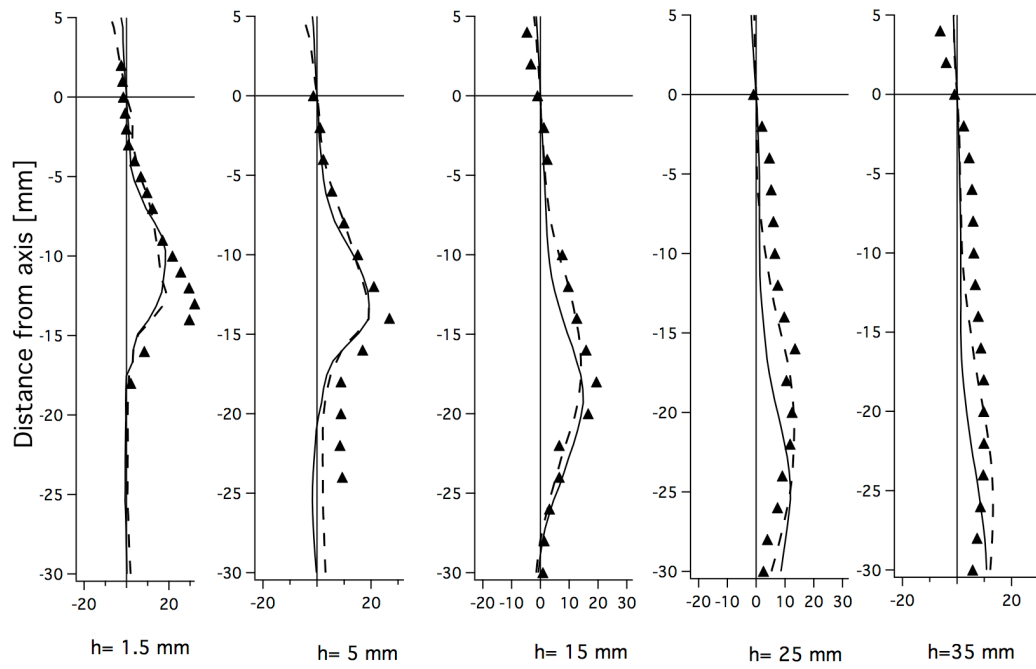


Fig. 22. Mean tangential velocity profiles for the 'pulsating' flame ($\phi = 0.7$) at five sections in the chamber. The experimental results (symbols) are compared to numerical results: perfectly premixed simulation (case C - solid line) and non perfectly premixed simulation (case D - dashed line).

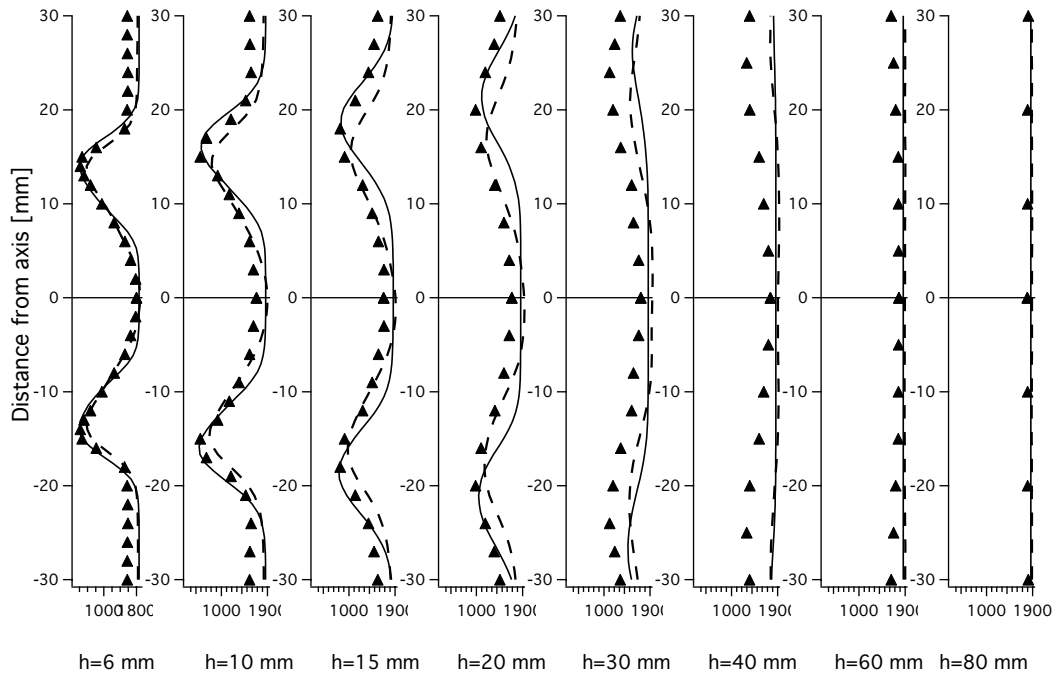


Fig. 23. Mean temperature profiles for the 'pulsating' flame ($\phi = 0.7$) at eight sections in the chamber. The experimental results (symbols) are compared to numerical data: perfect premixed (case C - solid line) and non perfect premixed simulation (case D - dashed line).

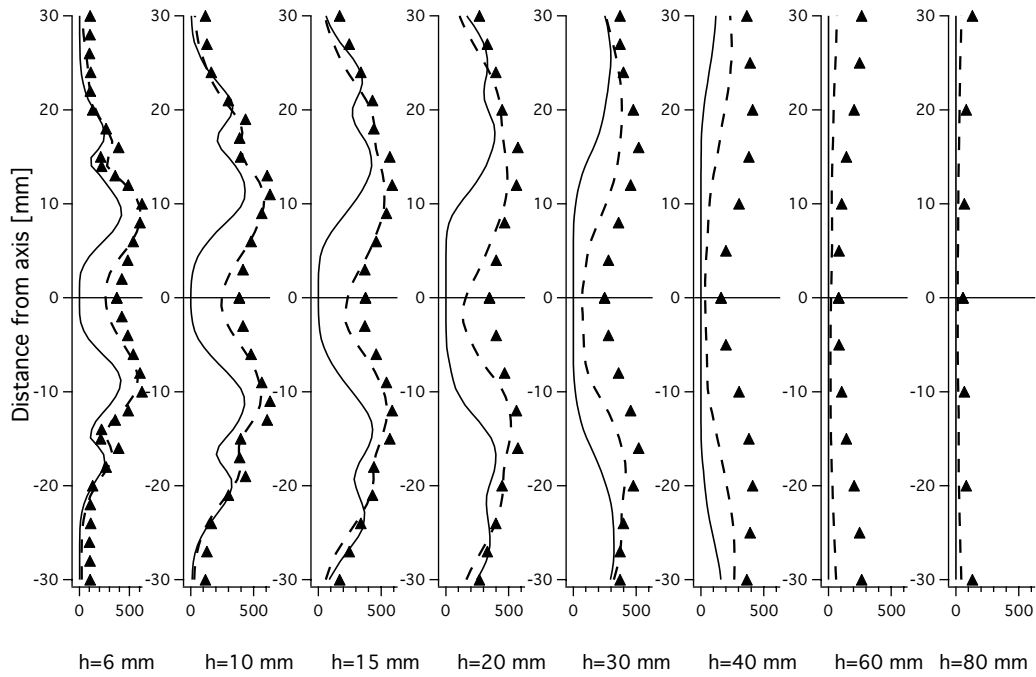


Fig. 24. RMS temperature profiles for the 'pulsating' flame ($\phi = 0.7$) at eight sections in the chamber. The experimental results (symbols) are compared to numerical data: perfect premixed (case C - solid line) and non perfect premixed simulation (case D - dashed line).

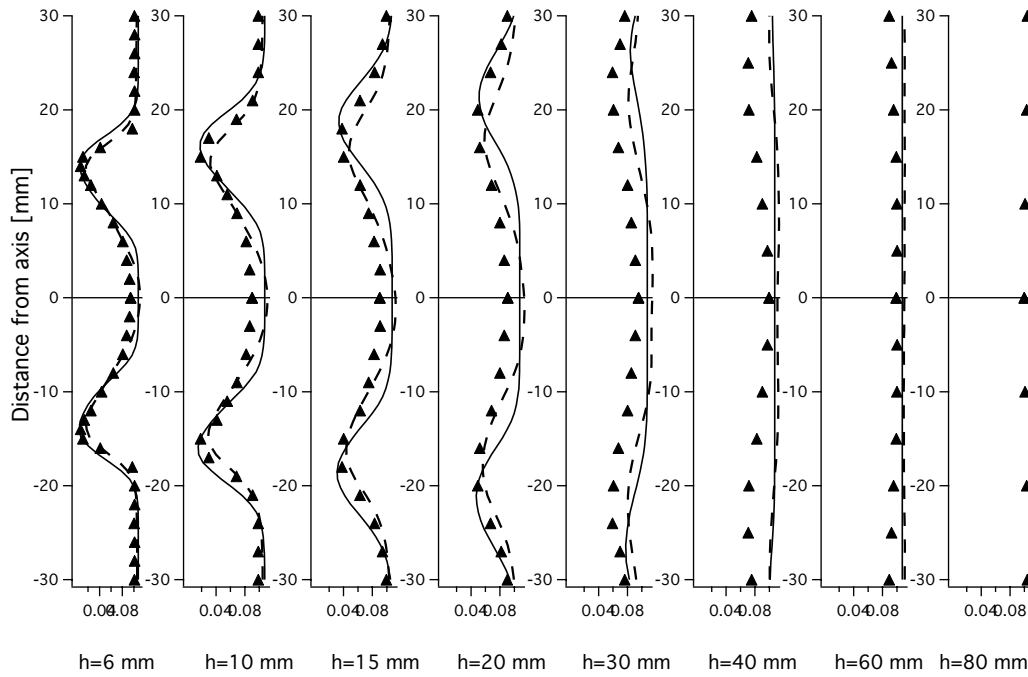


Fig. 25. Mean CO_2 profiles for the 'pulsating' flame ($\phi = 0.7$) at eight sections in the chamber. The experimental results (symbols) are compared to numerical data: perfect premixed (case C - solid line) and non perfect premixed simulation (case D - dashed line).

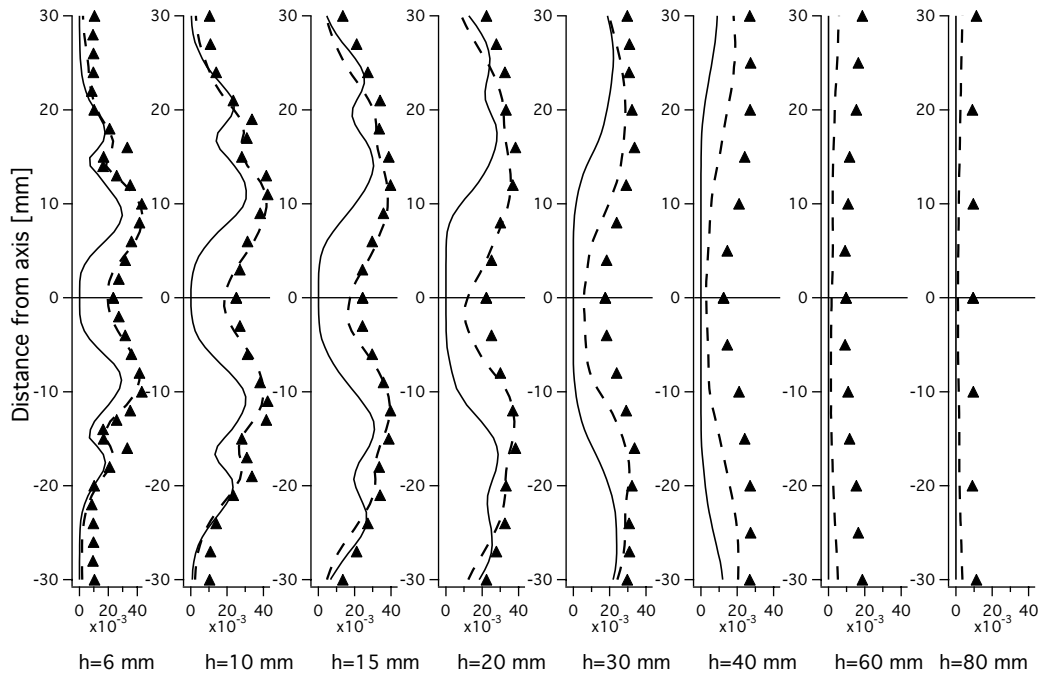


Fig. 26. RMS CO_2 profiles for the 'pulsating' flame ($\phi = 0.7$) at eight sections in the chamber. The experimental results (symbols) are compared to numerical data: perfect premixed (case C - solid line) and non perfect premixed simulation (case D - dashed line).

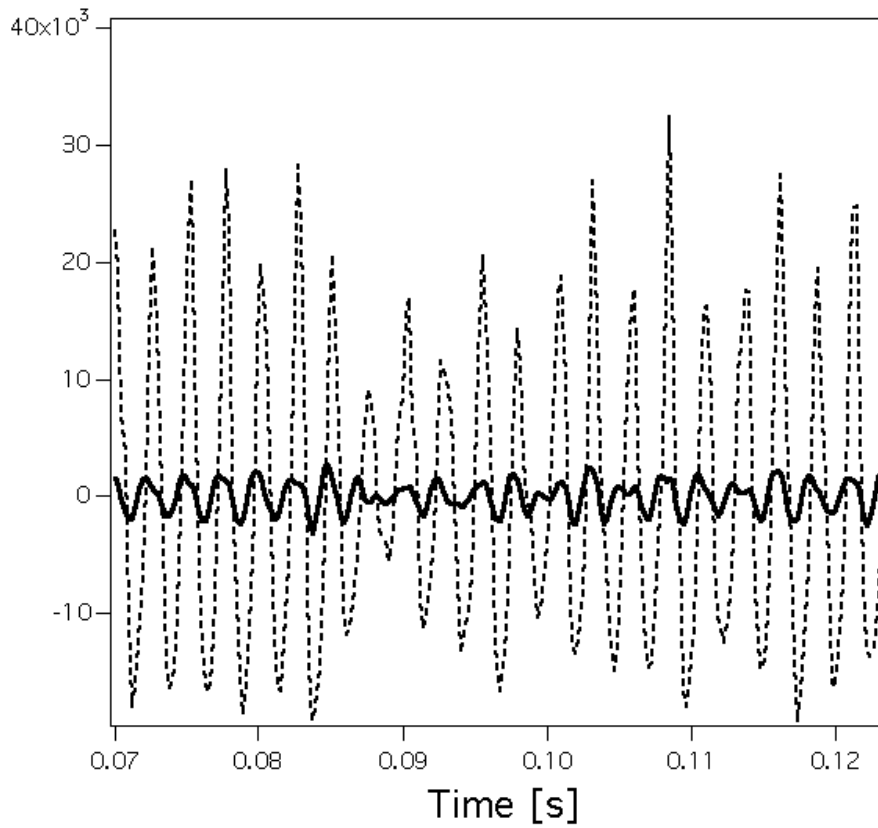


Fig. 27. Temporal evolution of the fluctuations of chamber pressure p_C (solid line, probe C in Fig. 1) and total heat release q (dashed line) for the 'pulsating' flame (case D).

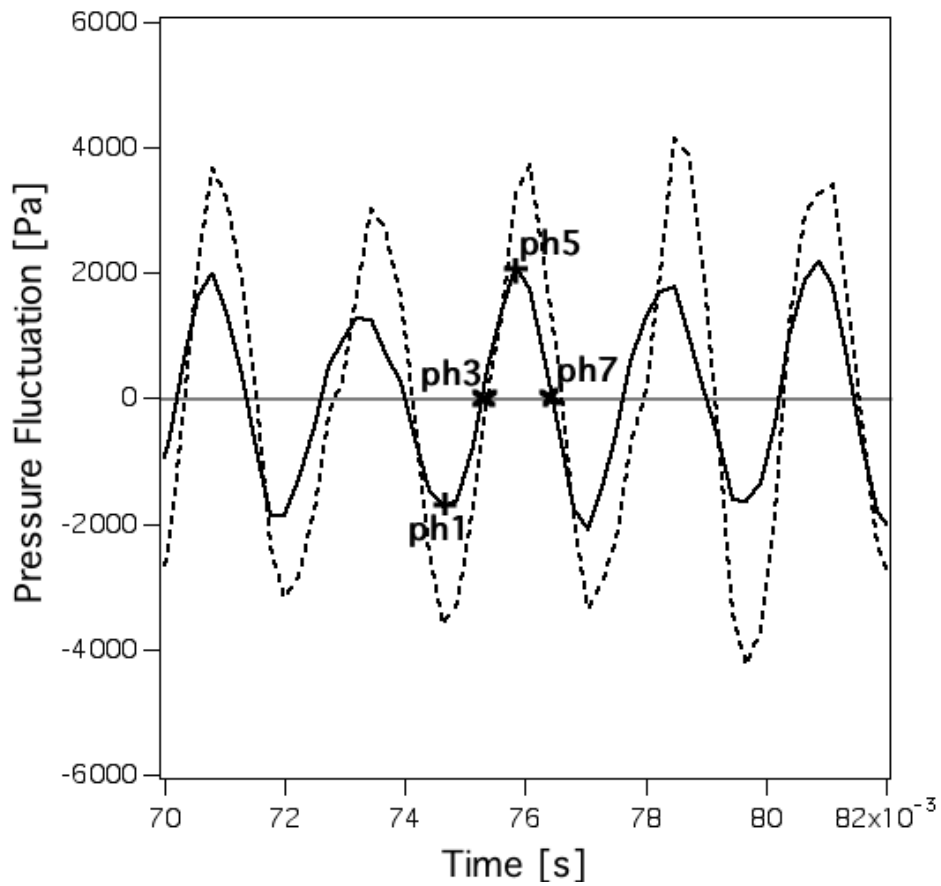


Fig. 28. Temporal evolution of the plenum pressure P_P at probe P in Fig. 1 (solid line) and the pressure drop ΔP (dashed line) between plenum and chamber (probe C in Fig. 1) for the 'pulsating' flame (case D).

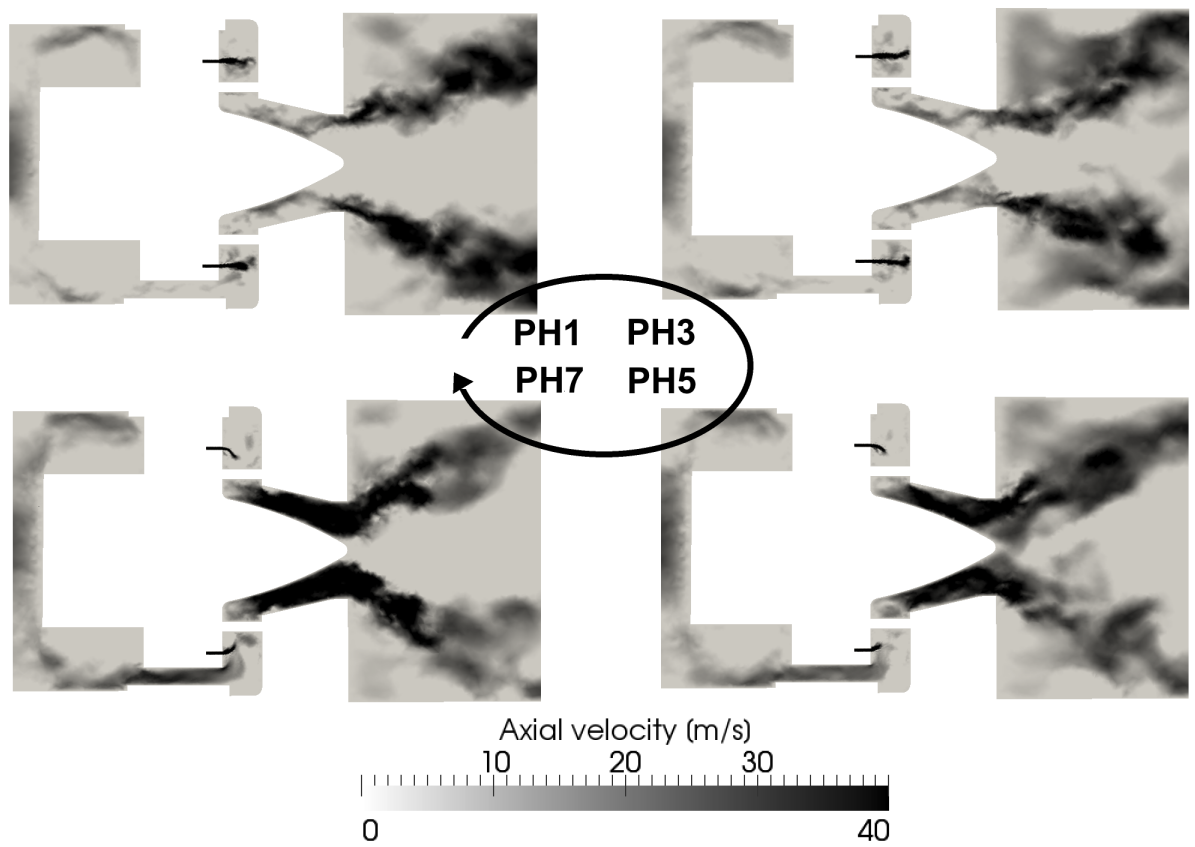


Fig. 29. Phase-locked instantaneous axial velocity fields for four different phases $ph1$, $ph2$, $ph3$ and $ph4$ for the 'pulsating' flame ($\phi = 0.7$, case D).

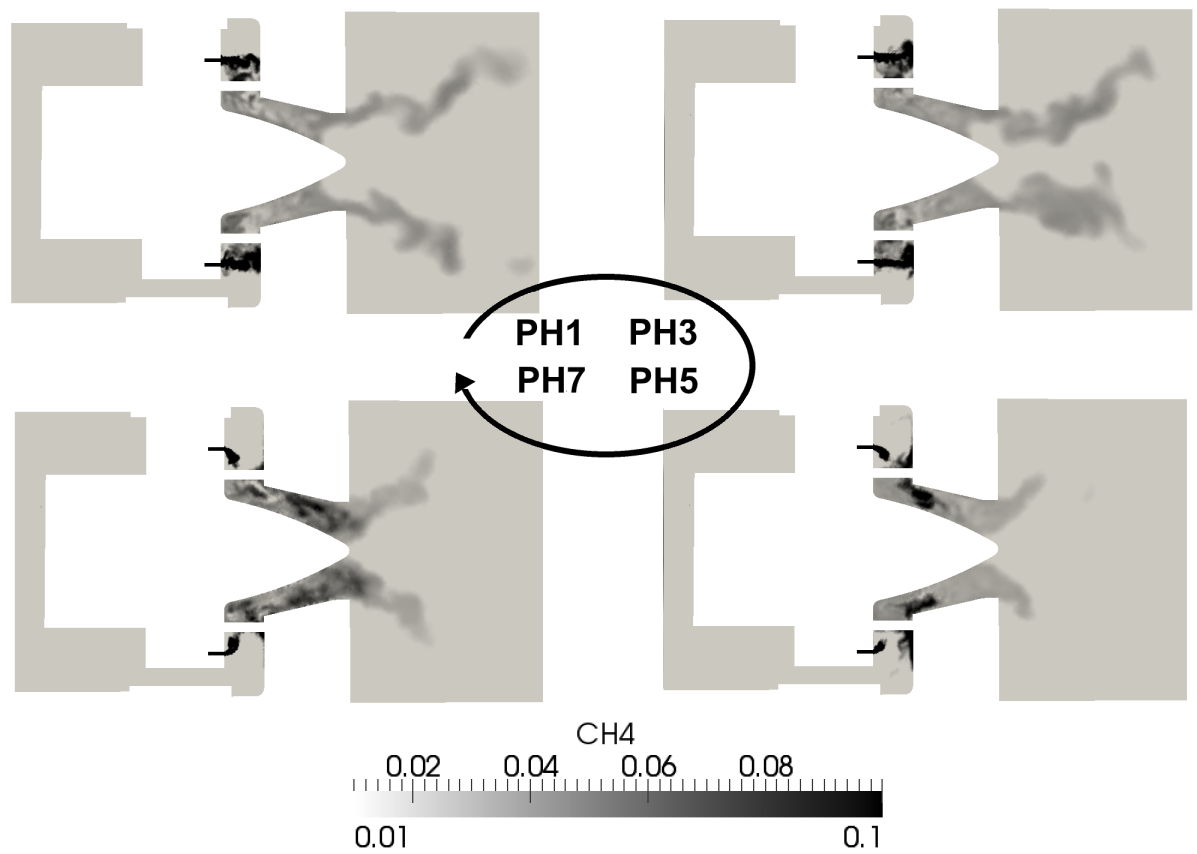


Fig. 30. Phase-locked instantaneous CH_4 mass fraction fields for four different phases $ph1$, $ph2$, $ph3$ and $ph4$ for the 'pulsating' flame ($\phi = 0.7$, case D).

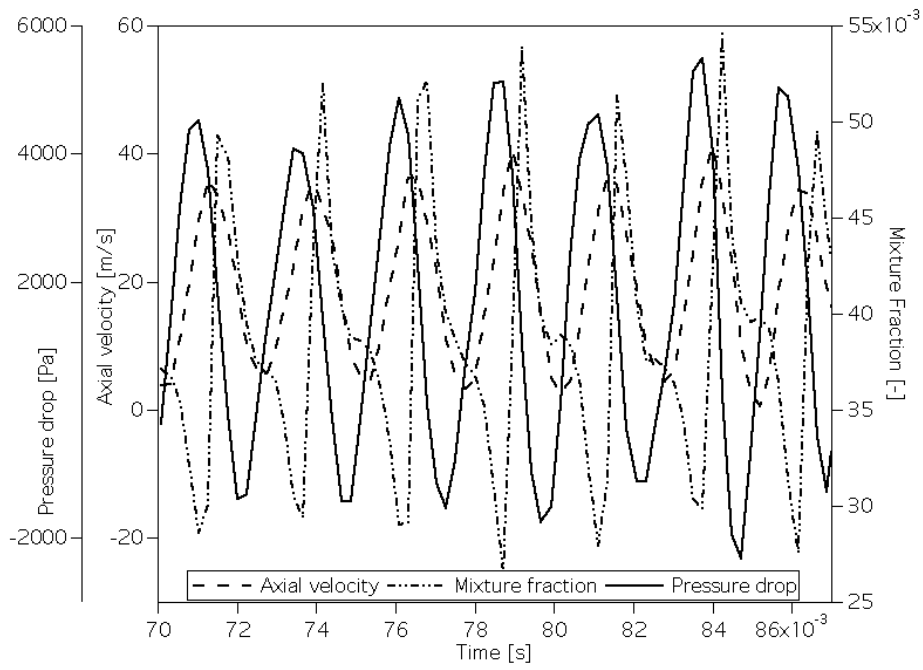


Fig. 31. Temporal evolution of the pressure drop (solid line), axial velocity (dashed line) and mixture fraction (dotted-dashed line) in the swirler (probe I) for the 'pulsating' flame ($\phi = 0.7$, case D).

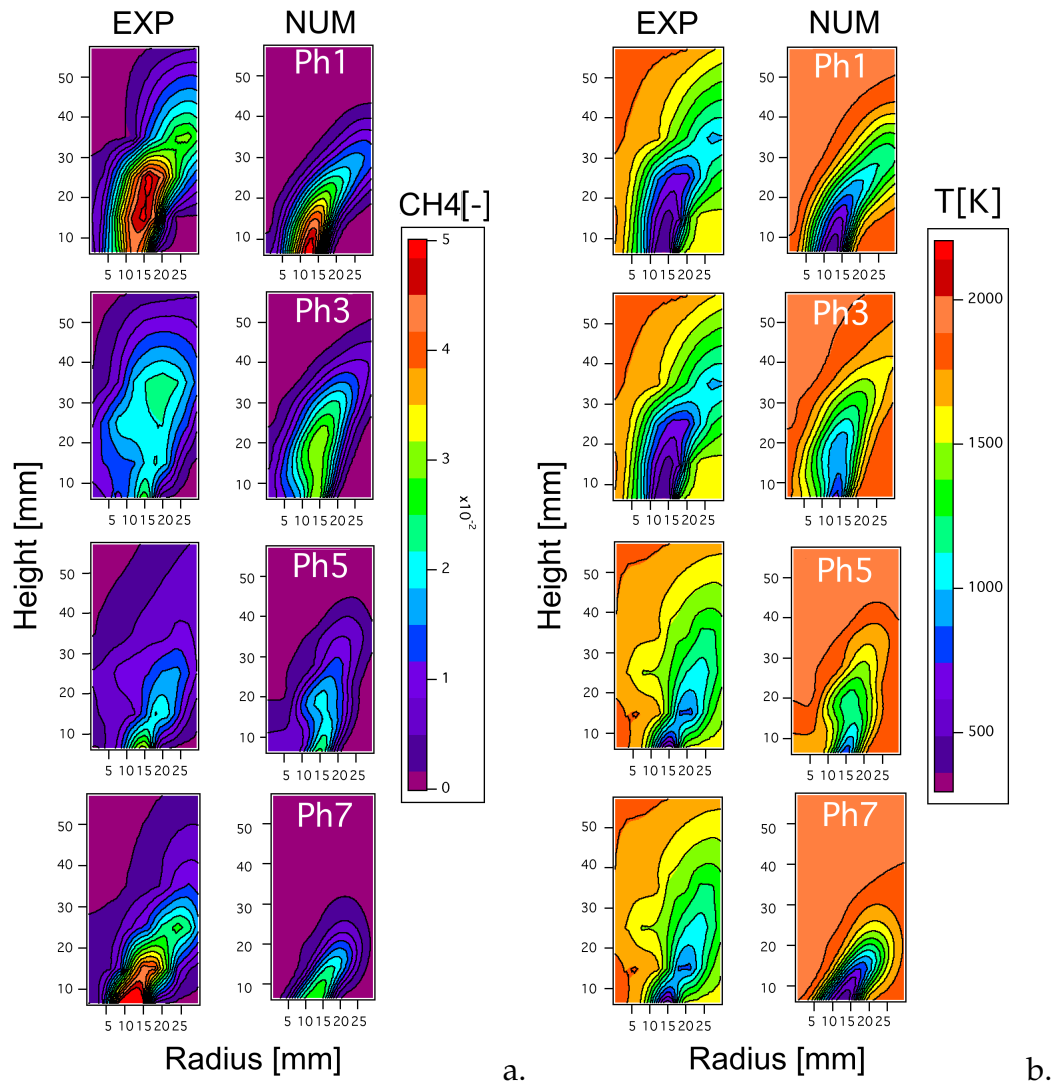


Fig. 32. Phase-locked mean fields of CH_4 mass fraction (a.) and temperature (b.) in the chamber (visualization window displayed in Fig. 1, dashed line). Comparison between experiments (left, case1) and numerical simulation (right, case D) for the 'pulsating' flame ($\phi = 0.7$).